# A Non-Gradient Heuristic Topology Optimization Approach Using Bond-Based Peridynamic Theory

by

Ahmed Abdelhamid
B.Tech., Higher College of Technology, 2012

A Thesis Submitted in Partial Fulfillment
of the Requirements for the Degree of

MASTER OF APPLIED SCIENCE

in the Department of Mechanical Engineering

# SUPERVISORY COMMITTEE

A Non-Gradient Heuristic Topology Optimization Approach Using Bond-Based Peridynamic Theory

by

Ahmed Abdelhamid

B.Tech., Higher College of Technology, 2012

**Supervisory Committee**

Dr. Afzal Suleman, (Department of Mechanical Engineering)
**Supervisor**

Dr. Ben Nadler, (Department of Mechanical Engineering)
**Departmental Member**

# ABSTRACT

**Supervisory Committee**

Dr. Afzal Suleman, Department of Mechanical Engineering
**Supervisor**

Dr. Ben Nadler, Department of Mechanical Engineering
**Departmental Member**

Peridynamics (PD), a reformulation of the Classical Continuum Mechanics (CCM), is a new and promising meshless and nonlocal computational method in solid mechanics. To permit discontinuities, the PD integro-differential equation contains spatial integrals and time derivatives. PD can be considered as the continuum version of molecular dynamics. This feature of PD makes it a good candidate for multi-scale analysis of materials. Concurrently, the topology optimization has also been rapidly growing in view of the need to design lightweight and high performance structures. Therefore, this thesis presents the potential for a peridynamics-based topology optimization approach. To avoid the gradient calculations, a heuristic topology optimization method is employed. The minimization of the PD strain energy density is set as the objective function. The structure is optimized based on a modified solid isotropic material with a penalization approach and a projection scheme is utilized to obtain distinct results. Several test cases have been studied to analyze the suitability of the proposed method in topology optimization.

# CONTENTS

# LIST OF TABLES

# LIST OF FIGURES

# ACKNOWLEDGMENTS

I would like to thank Dr. Afzal Suleman, for his patience, guidance, support, encouragement, and presence. For being a father figure, a mentor, and a unique person I would love to know and work with for the rest of my life.

I would like to acknowledge Abdolrasoul Sohouli and Nima Tofighi and my other colleagues at the Center for Aerospace Research for their valuable advice and suggestions on topology optimization that have enriched my experience at the University of Victoria.

I would like to mention Dr. Erkan Oterkus, for the valuable advice and for answering my questions in the many emails despite the fact that the ocean separates us and neither of us have met in person.

I am grateful to my idol, my father, Osama Aly, for expecting much from me and believing on me, along with my sister, Mentallah; my brother, Abdelrahman; my nieces, Manal and Aisha for being in my life.

Last but not least, a depth of gratitude to my wife, Yasmin Hassan, for her patience and encouragement, and for being a part of me.

# DEDICATION

This thesis is dedicated to my father, Osama Aly; and my mother, Manal Mohammed

# NOMENCLATURE

| | |
|---|---|
| PD | Peridynamic theory |
| CCM | Classical Continuum Mechanics |
| FEM | Finite Element Method |
| FD | Finite Difference method |
| PDEs | Partial Differential Equations |
| DG | Discontinuous Galerkin method |
| CG | Continuous Galerkin method |
| CE | Classical Elasticity theory |
| SPH | Smoothed Particle Hydrodynamics method |
| MD | Molecular Dynamics |
| XFEM | Extended Finite Elements Method |
| CZM | Cohesive Zone Model |
| FGMs | Functionally Graded Materials |
| ADR | Adaptive Dynamic Relaxation technique |
| COC | iterative Continuum-based Optimality Criteria |
| SIMP | Solid Isotropic Material with Penalization |
| IMB | Implicit Moving Boundary |
| SLP | Sequential Linear Programming |
| ESO | Evolutionary Structural Optimization method |
| BESO | Bidirectional Evolutionary Structural Optimization method |
| PTO | Proportional Topology Optimization method |
| EFG | Element-Free Galerkin method |
| MLPG | Meshless Local Petrov-Galerkin method |
| GA | Genetic Algorithm |
| SA | Simulated Annealing |
| H | Family members within a horizon |
| $\delta$ | Horizon radius |
| x | Position victor before deformation |
| y | Position victor after deformation |

| | |
|---|---|
| s | Bond stretch |
| $t_{(k)(j)}$.or $t_{(j)(k)}$ | Force density vector |
| $\underline{Y}$ | Deformation vector state |
| $\underline{T}$ | Force vector state |
| t | Time |
| u | Displacement |
| $u^*$ | Initial displacement |
| w | Scalar-valued micropotential |
| W | Strain energy density |
| L | Lagrangain L |
| TE | Total kinetic energy |
| U | Total potential energy |
| V | Volume |
| ρ | Density |
| $\dot{u}$ | Velocity |
| $v^*$ | Initial velocity |
| $\ddot{u}$ | Acceleration |
| $H^*$ | Displacement gradient |
| $L^*$ | Velocity gradient |
| $T^s$ | Surface traction |
| A | Area |
| Δ | Grid size |
| b | Body force |
| P | Point load |
| p | Distributed pressure. |
| C | Auxiliary parameter |
| F | External load |
| f | Force density vector of the pairwise response function |
| k | Bulk modulus |
| $\alpha$ | Coefficient of thermal expansion |
| $\sigma$ | Cauchy stress component |

| | |
|---|---|
| $\theta$ | Dilatation (average value of volumetric strain) |
| $T_{(k)}$ | Temperature change |
| $b_c$ | Peridynamic parameter |
| $a$ | Peridynamic parameter |
| $a_2$ | Peridynamic parameter |
| $a_3$ | Peridynamic parameter |
| $\mu$ | Shear modulus |
| E | Modulus of elasticity |
| c | Bond function |
| $c_0$ | Constant bond function |
| $c_1$ | Conical bond function |
| h | Thickness |
| $\zeta$ | Normal strain |
| $v_c$ | Volume correction factor |
| $\Delta t$ | Time step size |
| $c_d$ | Damping coefficient |
| K | Stiffness matrix |
| $\overline{V}$ | Volume fraction |
| $P_n$ | Penalization coefficient |
| RM | Remaining material amount |
| q | Proportion exponent |
| $\varphi$ | Density design variable |
| $\varphi^{new}$ | Density passing to the next optimization iteration |
| $\varphi^{prev}$ | Density in the previous optimization iteration |
| $\varphi^{opt}$ | Density in the current optimization iteration |
| R | Filter radius |
| $\gamma_{kj}$ | Filter weight |
| $\widehat{\varphi}$ | Filtered density |
| $\vartheta$ | History coefficient |
| $\eta$ | Projection parameter |

| | |
|---|---|
| $\beta$ | Projection parameter |
| $D_t$ | Discreteness |

# 1 INTRODUCTION

## 1.1 Peridynamics

The Peridynamic theory (PD) was first introduced into the computational mechanics field by Silling et al. [1] [2] as a nonlocal theory. The theory does not concern stress or strain and it is considered as a reformulation of the Classical Continuum Mechanics (CCM). The existing non-locality in the PD integro-differential equation of motion establishes the relationship between CCM and molecular dynamics for the purpose of predicting deformations with discontinuities. This accounts for long-range force effects and modelling of different length scale structures. Similarly, other nonlocal continuum theories have been introduced by Kroner [3], Rogula [4], Eringen and Edelen [5] and Kunin [6].

The state-based PD was first introduced by Silling et al. [2] to generalize the original PD theory "bond-based PD" [1] due to the assumption of the parallel and equal magnitude of the pairwise interactions. Additionally, this generalization seeks to find a solution for the inability to distinguish between the volumetric and distortional deformations [7]. This assumption resulted in limitations on the Poisson's ratio to be one-fourth and one-third for isotropic and homogenous materials for three-dimensional and two dimensional models, respectively. In addition to both bond-based and ordinary state-based PD theories, a non-ordinary state-based PD theory was developed to remove any central force restrictions and was used to solve transient dynamic solid mechanics problems [8].

Another generalized PD model called "micropolar PD" was proposed to model composite structures in [9] and to overcome any Poisson's ratio limitations. This PD model was performed within FEM to guarantee an effective application of boundary conditions. It was achieved by introducing PD frame elements and the micropolar PD stiffness matrix. PD moment was considered; FEM discretization was used; and degree of freedom reduction techniques were proposed.

Several applications of the PD theory have been discussed in the open literature. In the following sections, a description of various applications and the associated development of the PD theory are presented.

### 1.1.1 Analytical Solutions

The nonlinear integro-differential equation of motion in the PD theory contains spatial integrals and time derivatives in order to permit discontinuities and it is usually difficult to be solved analytically. Nevertheless, a few analytical solutions have been reported in the literature [10-13].

An approach proposed solving for a new viscoelastic model analytically by deriving the integral-representation formulas using the Fourier and Laplace transforms and Green's function in [10]. Another framework introduced a method to obtain analytical solutions from the formal analytical solutions in [11] similar to Weckner et al.'s approach from [12]. In this method, the divergent integrals from the formal Fourier transform solutions were renovated into generalized functions with convergent integrals.

### 1.1.2 Coupling in PD

The ability of allowing discontinuities is quite a distinct characteristic in PD. However, it is computationally expensive compared to other methods. Here, coupling between methods is considered to address the computational burden related to the PD method. A number of coupling techniques have been proposed in the literature [14-23].

An attempt to couple the PD theory and the Finite Element Method (FEM) to reduce the computational cost while proposing a model that allows discontinuities was presented in [14]. The model was divided into two sub-regions; the sub-region expected to experience a failure implements the PD theory while FEM was utilized in the opposite sub-region. An interface region establishes the connection between both the sub-regions. Interface elements were the key aspect of the coupling procedure and were used to calculate the coupling force. Using a similar technique, another PD-FEM model was proposed in [15]. The PD sub-region was discretized into hexahedral shaped zones, each containing material points. This technique results for a faster process of finding family members (an attempt to

reduce the computational cost by looking for family members only within the nearest zones). An overlap region was introduced as the region containing both finite elements and PD material points. In this zone, coupling equations were defined to calculate the velocity and displacement using FEM and body forces using PD.

Many other coupling approaches between the local and nonlocal theories have been reported. The Finite Difference (FD) method is known as an efficient modelling scheme of force wave propagation through a medium. Unlike the previous coupling schemes, the FD-PD model was proposed to improve and refine wave propagation while allowing crack initiation and growth [16]. A brittle elastic model for a fracture problem was developed using the same technique from the previously explained coupling schemes. PD was implemented in regions expected to experience high deformation, and vice versa. Coupling equations were introduced into the interface zone with a reflection coefficient to help in the wave transition process between the two regions.

In [22], a coupling approach between PD and partial differential equations models (PDEs) was proposed. Each method was assigned to a region: a failure region, a failure neighboring region, and an off-failure region. Regions were assigned: FEM-based Discontinuous Galerkin discretization method (DG) for PD, FEM-based Continuous Galerkin discretization method (CG) for PD, and FEM based CG discretization method for PDEs, respectively.

Coupling between nonlocal and local continuum mechanics was proposed in [17]. A flexible model based on morphing the constitutive weighted parameters in a morphing zone (interface zone) was developed. The transformation of any method in the morphing zone into either local, nonlocal or even hybrid depending on the necessity was achieved by creating functions relying on the strain energy equivalence techniques.

A PD coupling approach using the “variable horizon” technique was presented to serve the intent of coupling the nonlocal PD with the local PD to obtain a greatly reduced computational cost [18]. This technique changes the horizon size for each material point depending on its position within the model. Due to the condition difference, “ghost force”

phenomenon was developed. However, it was solved by modifying the PD equilibrium equations. In contrast, a PD model that permits the variable horizon technique without the production or elimination of ghost forces was proposed in [24].

Another coupling approach between local and nonlocal schemes was presented in a Classical Elasticity theory (CE)-PD model [19]. A blending technique was proposed to produce a derived force-based blended model that couples both the theories. Weighted terms were used to permit length scale variability and blending functions to exhibit better-uninterrupted performances for dissimilar methods.

Unlike PD, Smoothed Particle Hydrodynamics (SPH) method is mostly used in the fluid dynamics field; both are meshless and nonlocal methods. PD-SPH models were introduced twice in the literature. In [20], a simulation of a soil fragmentation induced by buried explosion shock waves was proposed. A field of consistent multi-bodies model mimicked the contact of the different mediums and a force transfer mechanism between the different types of particles was demonstrated, e.g. the approach treated a SPH point inside a PD horizon as a PD material point. Additionally, an artificial viscosity function and virtual particles were inserted into the model to control the nonphysical penetration and to ensure the numerical accuracy. In a similar simulation, [21] proposed a coupling algorithm that equates both the methods at the interface zone, e.g. influence functions and shape tensors from PD were constructed into SPH. Therefore, particles from the different types did interact with each other by giving the right contribution and translating any form of force into the equivalent form.

### 1.1.3 PD Convergence

PD convergence techniques have been seldom discussed in the open literature [25-27]. Convergence of PD stress tensors in an elastic material model as a function of downscaling the horizon was proposed in [25]. Stress tensors from a local PD model were converged to the local Piola-Kirchhoff stress tensor by considering assumed differentiable functions in PD to describe the local stress-strain relation. Also, reference [26] discussed and compared three types of convergence techniques to the local classical theory as the horizon approaches to zero. These techniques represent different relations between the horizon size

and ratio between the horizon and the volume of a point. Additionally, various bond functions were discussed. Another recent convergence study claims to prove that PD lack accuracy due to issues in the underlying theory [27], e.g. contributions of material points near the horizon's boundary are rough approximations. These approximations require further improvements by either implementing a volume calculation convergence algorithm called the "partial volume" algorithm or by using the "smooth influence functions" described in [28].

### 1.1.4 Multiscale Modelling

In [29] and [30], a theoretical overview of PD effectiveness in multi-scale modeling was presented. PD has been used commonly in multi-scale studies [31-36] due to its progressive failure modelling ability.

The capability of PD equation to permit long-range forces supports modeling nanoscale bonds in a one-dimensional strings of continues fibers, as presented in [31]. PD long-range forces were employed as the natural van der Waals forces. Due to the strong singular nature of van der Waals forces, it was stated that van der Waals forces could be present only between particles located in different parts of a body or between particles on different bodies, but not neighbors [37]. In a similar example of nanofibers and their networks [32], non-damageable bonds representing the van der Waals forces were implemented to allow interactions between different points in different fibers within a fiber network without horizon limitations. Furthermore, since the experimental testing of thin films is computationally expensive and tedious in few cases, a PD nanoscale model was presented in [33]. The study models fractures and wear of amorphous carbon films. Potential force functions from the Molecular Dynamics (MD) method were used in PD instead of the long-range forces in order to obtain more accurate deformations. In [34], PD was implemented to model a granular material to examine grains interactions and fractures. The PD mesoscale model was found to be superior to the Eulerian method in terms of the physical treatment.

Although MD as a nonlocal theory share many similarities with the PD theory, both methods are constructed based on different length scales. PD theory is best to describe

macro and micro scale, while, MD is the best to describe micro and nanoscale. A PD model was tested to act as an improved MD model in [36]. Higher-order gradient models were derived from both methods and compared. The comparison proved that PD can be considered a computationally cheaper and improved Lennard-Jones MD. MD characteristic properties were also proven to be presented in the PD theory unlike CCM. Furthermore, PD was found to be a perfect alternative to MD in large scale models by introducing graining technique [35]. A three-staged graining process consisted of: first, atoms and their pairwise interaction forces were distributed randomly into the PD model; second, achieving model's homogeneity; finally, upscaling procedure of the PD horizon in the equation of motion.

## 1.2 Applications

### 1.2.1 Mechanical and Failure Applications in PD

Crack propagation and fractures models using PD are introduced regularly in the literature. Atomistic, lattice models were usually used for simulating dynamic cracks, but PD point of strength is the ability to work without the need of the spatial derivative of the displacement components.

In [38], a PD model was introduced to implement a crack growth in a dynamic problem. The "bond stretch" definition was introduced and discussions regarding the selection of the grid size and the horizon size, and stability conditions such as the time step size were proposed. Moreover, the implementation of dynamic fracturing for a PD visco-plastic material model was proposed in [39]. In PD, a crack is defined as the correspondent action of a bond failure; failure is represented based on the critical energy density criterion. This criterion eased fracture principles without considering crack laws.

The relation between stress waves and fractures in PD models was investigated and compared to the theoretical mechanisms of branching [40]. PD's accurate ability to capture fracture characteristics was explained by studying the strain energy dissipation and the bonds between material points. As the experimental studies of cracks and fractures offer a large description of their characteristics, a PD model in [41] was able to generate the same

experimental characteristics. The model described the crack branching phenomena and the effect of the load. Additionally, it explained the increase of crack path instability (a dependent of crack propagation speed [42]), and tested the trail asymmetries about pre-crack lines.

Dynamic cracks in brittle materials were discussed and detailed in [43]. Different micro-modulus functions were employed and tested. The formation of crack branches in PD was proven to be dependent on the high rate of crack propagation speed, exactly as observed in experimental tests. In [44], a model proposed the relation between the horizon size selection and crack branching. In contrast to [43] and [41], the size of the horizon was found to be not largely affecting the crack propagation speed, and likewise under few conditions, branch angles were found to be not affected. Also in [23], a brittle fracture study of rock-like materials was presented. A PD-FEM coupled model was used to study the formation of both secondary shear cracks and tensile wing cracks around pre-notched flaw inclination angles.

In [45], a comparative study between PD, extended finite elements method (XFEM) and a cohesive zone model (CZM) was proposed. Several cases of dynamic fracturing and crack growth were applied. In all simulations, results were found to agree with the observed experimental results including time and velocity, but CZM and XFEM failed in predicting small branches. Upon closer inspection of PD, it was predicted that the efficiency of PD will not only help predicting, but also in explaining the branching phenomena.

An adaptive refinement technique for the grid in a PD crack propagation model was proposed in [46]. The technique implemented multiple zones in which the grid size in each zone differ from another based on the expected crack path. Due to the interaction of these different scaled regions, errors and energy flux distortion were expected to occur and were solved. PD was also able to describe different cases of bio-material fractures in [47]. A force function for the bio-material model was introduced and a PMMA bio-material plate was implemented.

In [48], an application of bond-based PD in plain and reinforced concrete structures was introduced. As material points along a boundary of a model have less interactions, therefore, have less stiffness, the resulting unneeded boundary effects were minimized by introducing virtual material points along the boundary called “ghost nodes”. In addition, various volumetric patterns for material points were tested to improve isotropy and Poisson’s ratio along the model. In [49], PD models were also introduced to study the damage and failure of concrete columns under uniaxial compression. A PD three-dimensional rectangular concrete plate model was introduced to examine the capability of accomplishing tension, compression and impact cases in [50]. A pairwise force function was created; the developed simulations were found to be outstanding. In [51], Fiber reinforced concrete structures were modeled using the non-ordinary state-based PD. To create random orientation of fibers, some material points were dispersed into a domain while each assigned to represent a midpoint of a fiber. These points select random angles and starts to grow in two opposite directions. In addition, a modeling scheme proposed as “semi-discrete fiber modeling method” was used to compute the fiber forces and then convey it into the matrix particles.

The creation of a bond-based PD fracture model for functionally graded materials (FGMs) was proposed in [52]. Few parts in the PD formulation were modified to help defining the composite type of material and to adjust the interactions between material points with different material properties inside the domain. Furthermore, it was observed that not only the loading conditions but also the loading time affect the crack path. Crack propagation, path, and growth were determined to be dependents of stress and elastic wave reflections. In [53], bond-based PD fracture models for orthotropic and transversely isotropic materials were introduced to determine and capture crack behavior.

An application of a progressive microscopic stress-corrosion cracking in PD for high-strength low-alloy steel was proposed in [54]. Formulation of hydrogen diffusion based on the Fisher model was implemented into PD to represent the chemical corrosion. This implementation coupled the chemical diffusion model and the mechanical model. Main steps include the introduction of load, hydrogen spreading into material regions, coverage predictions, material-hydrogen interactions, crack propagation predictions and hydrogen

re-spreading. In [55], a subsurface corrosion damage PD model was proposed. Coupling between the solid system and the electrolysis process was controlled by virtue of a phase changing mechanism that describes the anodic reactions inside the domain.

PD Fatigue models were also proposed in the literature. In [56], an approach presented a model without the use of external controllers. The proposed model had the ability of simulating the crack growth but not the crack initiation. Fatigue failure was represented by decreasing the critical stretch value of the bonds near to the pre-existing cracks with the increase of load cycles. In contrast to [56], in [57] a variable controller called "remaining life" was introduced into the bond formulation to represent the damage resisting capacity of each bond. This variable changes due to the cyclic loading over time. Another PD fatigue model was proposed using a method called "energy minimization conjugate gradient" to solve for static solutions based on minimization of the strain energy [58].

A standard that describes failure in PD was proposed in [59] after approaching an energy based failure technique. Based on thermodynamics, this technique resolves for determining the required amount of energy by a bonds in order to break. To demonstrate the damage in terms of energy, the technique requires information about the number of broken and unbroken bonds for each material point.

The use of PD have been extended in order to simulate fractures on a heterogeneous geological domain in [60]. The hydraulic fracturing process "fracking" is commonly used in natural gas wells. The proposed work discussed the failure process of a pre-fractured viscoelastic material model and the relation to both the angles of approach and the differential horizontal stress. The exact same material properties and characteristics of the natural domain such as shear slippage were introduced.

The first PD model used for structural design analysis to study, predict and simulate buckling failure was proposed in [61]. Two cases were implemented to study the influence of compression and temperature loads and factors such as cross-sectional area, boundary conditions, dimensions and material properties were tested.

Anti-plane shear and torsional deformation applications in PD were approached in [62]. Due to the loading conditions, the proposed scheme introduced a rework to the PD parameters and the PD equation of motion. Aside from that, critical stretch of a bond based on the critical strain energy release rate for tearing conditions was considered.

An analytical adjoint sensitivity analysis method based on the PD theory was introduced in [63] to solve brittle material crack propagation problems. Sensitivity equations were derived using the direct differentiation and the adjoint variable methods. Moreover, A PD framework was used in [64] to formulate a nonlocal cohesive model that is able to solve discontinuities. Forces and the strain energy were introduced similarly as in the PD theory. Material points represented the physical properties and a process zone was introduced as the region expected to fail. The selection of the horizon size in the cohesive model was found responsible for indicating how large the process zone is.

### 1.2.2 PD and Fiber-Reinforced Composites

In [65], a homogenization approach in PD for fiber-reinforced composite lamina was presented by matching the micro-scale PD strain energy, and elastic and fracture parameters to the classical composite macro-scale longitudinal and transverse strain energies, and the classical parameters. General analytical bond elasticity formulas were obtained without a need for any numerical evaluation of each grid at the beginning. Scaling factors were introduced in order to equate between the different scales. A similar approach proposed in [66] was used to simulate delamination and matrix damage in fiber-reinforced laminates. Unlike [65], the homogenization approach required a numerical evaluation for every grid to match the classical model after the initial discretization. In [67], an extension to [65] was proposed to enable the use of the homogenization approach when the discretization is uniform or not and while considering any orientation of the fibers. An algorithm was proposed to provide accurate scaling factors without depending on the grid size or the fiber orientation. In [68], PD models of composite laminates were proposed and solved without a homogenization process. Real material properties of both the fiber and matrix materials were used. Matrix and fibers were modeled individually as rectangular cross sections next to each other in a stacking sequence similar to a chess board. Note that

the elastic properties in matrix or fiber directions are the true elastic parameters of the matrix and fiber materials in contrast to [65] and [66]; where directional elastic properties of the homogenized lamina were considered.

Usually in PD laminate models, all bonds representing interactions between particles from different layers "interlayer bonds" within a single body have a constant critical stretch value. In [69], a technique introduced the calculation of variable critical stretch values for this type of bonds. This variation was considered by studying the effect of the local deformation on each bond. This helps in presenting variable energy release rates depending on different fracture modes. Moreover, a PD rate-dependent constitutive equation was introduced based on merging a microelastic brittle model and a viscoelastic Kelvin-Voigt model in [70]. The generated model used an energy release approach and implemented a time dependent critical stretch. Delamination, collision and penetration were proposed in impacting velocity cases.

A homogenized laminate model from [71] was introduced to extend the PD theory in modelling delamination. Four types of bonds were discussed and introduced to describe both in-plane and interlayer interactions while considering normal and shear interactions. In [72], an extension for the bond-based PD technique introduced in [73] to model fiber reinforced composites without Poisson's ratio restrictions was proposed. The extended model had the ability of evaluating stress and strain to use them in a failure criteria. In [74], to test the capability of PD, a laminate model was proposed to study high-velocity impact and explosive load responses. Delamination and matrix damage responses were discussed by reviewing the dependency of the interlayer damage and intralayer damage on the different types of interaction bonds.

### 1.2.3 PD and Fluids

In a few reported studies, PD models have been developed to simulate fluid flow. An implementation of PD to simulate a porous flow was proposed in [75]. Pore pressure effect standards and poroelastic medium response standards were adopted into the PD formulation for the solid model as well as producing PD fluid formulation for the fluid model. Another study introduced a PD flow model driven by a hydraulic potential field in

[76]. The PD model successfully replaces the classic framework of Richard's equation by defining flow density and power functions and driving the moisture's volumetric change rate, flux and flow power parameters.

## 1.3 Topology Optimization

Topology optimization or "numerical structural shape optimization" as it used to be known in the seventies has always been an interesting research area attracting the researcher's attention. In the last five decades, topology optimization has been rapidly growing and continuously developing. According to [77], the early topology optimization techniques adopt "sizing design variables", e.g. thickness and cross sectional areas. Although sizing design variables do not change the shape of the initial design structure, shape design variables do. Shape design variables were utilized to satisfy the objective function of the optimization problem by changing the boundary of the design structure. In such cases, the nodal coordinates of the FEM nodes along the boundary of the design model could be the design variable.

### 1.3.1 Topology Optimization Methods

A topology optimization approach based on a homogenization method was first introduced in [78]. Materials with different properties were distributed inside the design space creating an anisotropic material, where its property was computed using the homogenization method. The main purpose behind introducing the approach was to avoid problems associated with the "boundary variations" techniques. To illustrate, it was stated that in boundary variations techniques element re-meshing is required and a similarity between the initial and final design structure may occur. The presentation of the homogenization method is large in literature; mainly in [79, 80].

The application of the iterative Continuum-based Optimality Criteria (COC) methods in layout optimization has been proposed frequently in the literature. Well-known approaches that implement the COC methods were presented in [81-83]. The approach was first introduced and the potential of performing a cross-section optimization and a generalized shape optimization was discussed in [81]. As the name of the method suggests, the

optimality criteria for a structure was obtained analytically from the variational methods. Based on the optimality criteria and an iterative FE method, real and fictitious structures were distributed within the model structure. This approach was proposed to perform a cross-section optimization in [82] and a generalized shape optimization in [83].

Solid Isotropic Material with Penalization (SIMP) method was first introduced in [83, 84]. In SIMP there were two main material regions within the model; solid regions and empty regions. Solid regions represent regions filled with material, and vice versa. A density dependent material property of each region was computed using different values of the penalized density. The main purpose behind introducing the SIMP method was to perform generalized shape optimization while avoiding the homogenization method. An additional modified SIMP approach was proposed in [85, 86]. In this approach, a material property limit was set to represent solid and empty material regions. Material regions with high density and high stiffness represent solid material regions, while material regions with zero density and low stiffness represent empty material regions (note that zero density does not reflect zero stiffness). Correspondingly, in the original theory, a single material property was used and the density was set between a slightly large number than zero to one.

The level set method or the Implicit Moving Boundary (IMB) method was proposed in [87] as a novel structural topology optimization approach. As the names suggest, the level set method optimizes a structure by moving its boundary using a scalar function called a level set function. In [88], a FD based IMB approach was proposed. It was stated that the function supports holes creation or merging and boundary movement according to the velocity of the boundary. Furthermore, a numerical procedure was developed using IMB for structural topology optimization [89]. In addition, a topology optimization approach called the sequential linear programming (SLP) level set method was proposed in [90]. It was stated that the proposed method permits having more than one constraint in addition to the ability of optimizing non-level set variables.

An approach called “bubble method” intended for topology and shape optimization was proposed in [91, 92]. This method optimizes a structure based on the classical shape

optimization of boundaries. When the objective function and the volume constraint were satisfied, a hole was inserted into the structure in an optimal position. Once again, another shape optimization was performed. Note that, the boundary of the hole and the structure were optimized simultaneously.

### 1.3.2 Non-Gradient Methods

In terms of the optimization strategy, topology optimization may be classified into a gradient-based and non-gradient optimization methods. As the name suggests, gradient-based methods require gradient calculations of the objective function and the constraints. On the other hand, non-gradient methods are usually used to overcome the complications associated with gradients calculation; especially stress gradients. However, the gradient information obtained by gradient-based methods is responsible for higher efficiency in terms of the speed required to archive an optimal solution from the optimization process. Few well-known examples of non-gradient methods are the Evolutionary Structural Optimization (ESO) method, the Bidirectional Evolutionary Structural Optimization (BESO) method and the Proportional Topology Optimization (PTO) method. In [93], a structural topology optimization approach based on the ESO method was introduced. During the nineties, the ESO was known as a straightforward simple density based method. In the proposed work, FEM was adopted and ESO was represented to rely on the concept of removing material regions subjected to the lowest stress. The ESO method is widely spread and discussed in the literature; especially in [94]. The BESO method was proposed in [95] as an extension of the ESO method. Although, a structural topology was modified based on the ESO method by removing material regions, the BESO method carryout modifications by adopting material addition and removal. In [96], both the ESO and the BESO methods were discussed in terms of the theory and the applications. Furthermore, the PTO method is proposed by Biyikli and To in [97]. In PTO, density is dependent on the objective value of the structure. Furthermore, a density dependent material property is computed for each element in each optimization iteration to distribute material within the structural model. The approach used in the PTO is similar to the approach in the SIMP method, although, the density of an element in the next optimization iteration is assigned according to its value in the current and the previous iterations.

### 1.3.3 Meshless Methods in Topology Optimization

Typically, the structural analysis method required for the topology optimization process utilize a local mesh-based solid mechanics method such as FEM and FD. Correspondingly, the presentation of non-local or meshless based solid mechanics methods is infrequent. As far as known, PD has not been used yet to carry out a structural analysis in a topology optimization problem. Meshless methods were found to be employed in the structural topology optimization in few occasions; the Element-Free Galerkin (EFG) method in [98-100]; SPH method in [101]; the Meshless Local Petrov-Galerkin (MLPG) in [102]. In mesh-based methods, a structural model may face mesh deformations under certain conditions, where, complex re-meshing is required. Accordingly, some meshless methods were better substitutes in terms of simplicity and efficiency.

### 1.3.4 Design Variable Classification

In addition to classifying the topology optimization methods based on the gradient, these method may be classified based on the design variable; discrete or continuous. The Genetic Algorithm (GA)[103, 104] and the Simulated Annealing (SA) optimization [105] method are two examples of topology optimization methods that utilize a discrete design variable. However, continuous design variables are more successful for topology optimization [106].

The mathematical basis of most computational methods assumes that a body will keep being continuous as the deformation occurs. For example in FEM, studying material failure has lagged behind because of its limited capabilities. When modeling a crack, most methods employ PDEs of CCM for a continuous body. At crack tips or along crack surfaces, having spatial derivatives in the PDEs is a limitation [1]. Thus, the mathematical structure fails at the moment a crack appears within a body. For that reason, other techniques were established to solve these limitations. Redefining structures to ignore cracks as they appear and prescribing crack condition as boundary conditions is one of the most used techniques. However, these methods suffer from the lack of crack growth standards and the requirement of re-meshing. Correspondingly, a MD-based method can solve these limitations. Although this atomistic method provides insight into the nature of

fractures, it is poor when modeling real-life structures [7]. Consequently, PD is a perfect scheme to model progressive failure in multi-physics and multi-scale problems.

At the present time, lightweight structures that possess a high structural performance are required in the various engineering fields. As a result, the research field of topology optimization is rapidly expanding.

Coupling between an efficient structural topology optimization scheme and PD lead to the creation of a simple-to-implement topology optimization method. Since PD permit and predict discontinuities, a powerful topology optimization method in accounting for such imperfections to improve the robustness of a design is the main aim.

## 1.4 Thesis Objectives and Layout

Every topology optimization scheme combines an optimization method and a structural analysis method. This thesis aims for the potential of a PD-based PTO approach. PD is a meshless nonlocal method; PTO is a non-gradient heuristic method that uses continuous design variables. In this work, a Heaviside-type projection operator is adopted and implemented to obtain distinct and robust results. Furthermore, this thesis provides a wide section of literature review to represent the background and the applications of PD.

This thesis is divided into three main sections. Chapter 1 presents and discusses the literature behind the methods employed in this work; Chapters 2 and 3 present the adopted methodologies; and Chapter 4 presents and discusses the results.

# 2 PERIDYNAMIC THEORY

The PD theory is first introduced into the solid mechanics field as a non-local meshless method that permit discontinuities. This chapter describes and fully adopts the peridynamic theory presented by Madenci and Oterkus in [7]. The chapter is divided into three main Sections. Sections 2.1-2.7 present the basics of the PD theory; section 2.8 illustrate the connection between PD and CCM; sections 2.10-2.16 discuss the numerical implementation of the PD theory.

## 2.1 Forces and deformation

In PD, every structure is discretized into many volumetric points. Material points interact with each other within a finite distance called the "horizon", δ. All material points within the horizon of point k are called "family members" of point k, $H_{(k)}$ as shown in Figure 1. PD defines the stretch relation between a point and its family member as

$$s_{(k)(j)} = \frac{(|y_{(j)} - y_{(k)}| - |x_{(j)} - x_{(k)}|)}{|x_{(j)} - x_{(k)}|}, \tag{1}$$

where $(j = 1,2,..,N)$ represents family members, $(x_{(j)}\text{-}x_{(k)})$ is the relative position vector before the deformation and $(y_{(j)}\text{-}y_{(k)})$ is the relative position vector after the deformation. As a result of the interaction between point $x_{(k)}$ and the family member $x_{(j)}$, a force density vector develop and is defined as the force applied by the family member $x_{(j)}$ on the point $x_{(k)}$, $t_{(k)(j)}$. Therefore, one can consider that the deformation of point $x_{(k)}$ depends on the deformation of all family members.

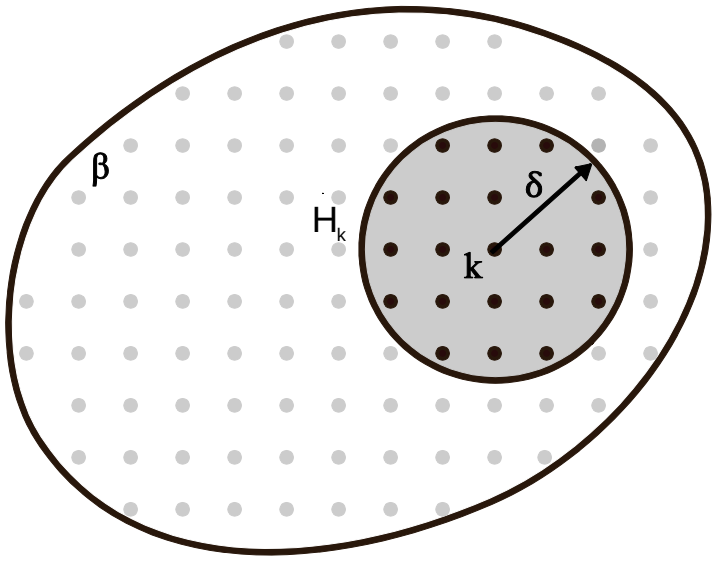


Figure 1: The family (H) of point k within the horizon radius **δ**.

According to the presented work in [2], the relative position vectors after deformation and force density vectors between point $x_{(j)}$ and all family members can be stored in two arrays, $\underline{Y}$ and $\underline{T}$, called "deformation vector state" and "force vector state", respectively

$$Y_{(x(k),t)}\begin{Bmatrix} y_{(1)} - y_{(k)} \\ \vdots \\ y_{(\infty)} - y_{(k)} \end{Bmatrix} \tag{2}$$

$$T_{(x(k),t)}\begin{Bmatrix} t_{(k)(1)} \\ \vdots \\ t_{(k)(\infty)} \end{Bmatrix}. \tag{3}$$

The relation between the relative position vectors before deformation and the relative position vectors after deformation in terms of the deformation vector state is expressed as

$$(y_{(j)} - y_{(k)}) = Y(x_{(k)}, t)\langle x_{(j)} - x_{(k)}\rangle, \tag{4}$$

and the force density vector between points $x_{(k)}$ and $x_{(j)}$ in terms of the force vector state is expressed as

$$t_{(k)(j)}\left(u_{(j)} - u_{(k)}, x_{(j)} - x_{(k)}, t\right) = T(x_{(k)}, t)\langle x_{(j)} - x_{(k)}\rangle, \tag{5}$$

where $u_{(j)}$ and $u_{(k)}$ are the displacement of points $x_{(k)}$ and $x_{(j)}$, respectively.

## 2.2 Micropotentials

A micropotential is a material property and stretch dependent component of the strain energy density. Each interaction develops pairwise scalar-valued micropotentials, $w_{(k)(j)}$ and $w_{(j)(k)}$, given in the form

$$w_{(k)(j)} = w_{(k)(j)}(y_{(1k)} - y_{(k)}, y_{(2k)} - y_{(k)}, \dots) \tag{6}$$

and

$$w_{(j)(k)} = w_{(j)(k)}\left(y_{(1j)} - y_{(j)}, y_{(2j)} - y_{(j)}, \dots\right), \tag{7}$$

where $y_{(1k)}$ and $y_{(1j)}$ are the deformed position vectors of the first family member to interact with point $x_{(j)}$ and point $x_{(k)}$, respectively. The strain energy density at point $x_{(k)}$, $W_{(k)}$, is expressed as

$$W_{(k)} = \frac{1}{2}\sum_{j=1}^{\infty}\frac{1}{2}\left(w_{(k)(j)}\left(y_{(1k)} - y_{(k)}, y_{(2k)} - y_{(k)}, \dots\right) + w_{(j)(k)}(y_{(1j)} - y_{(j)}, y_{(2j)} - y_{(j)} \dots)\right) V_{(j)}. \tag{8}$$

## 2.3 PD Equation of Motion

By defining the Lagrangain L as

$$L = TE - U, \tag{9}$$

where TE is the total kinetic energy and U is the total potential energy, defined as

$$TE = \sum_{i=1}^{\infty}\frac{1}{2}\rho_{(i)}\dot{u}_{(i)}.\dot{u}_{(i)}V_{(i)} \tag{10}$$

and

$$U = \sum_{i=1}^{\infty} W_{(i)} V_{(i)} - \sum_{i=1}^{\infty} (b_{(i)} . u_{(i)}) V_{(i)}, \tag{11}$$

where i is the number of the material point. Solving for the Lagrange's equation using the principle of virtual work, the integral form of the PD equation of motion obtained is written as

$$\rho(x)\ddot{u}(x,t) = \int_H (T(x,t)\langle x' - x\rangle - T(x',t)\langle x - x'\rangle) dH + b(x,t). \tag{12}$$

## 2.4 Initial Conditions

The initial displacement and the initial velocity is represented as

$$u(x, t = 0) = u^*(x) \tag{13}$$

and

$$\dot{u}(x, t = 0) = v^*(x). \tag{14}$$

The initial conditions for the displacement and velocity gradients, $H^*(x)$ and $L^*(x)$, respectively, are expressed as

$$u(x, t = 0) = u^*(x) + H^*(x)(x - x_{ref}) \tag{15}$$

and

$$\dot{u}(x, t = 0) = u^*(x) + L^*(x)(x - x_{ref}), \tag{16}$$

where $x_{ref}$ is the reference point.

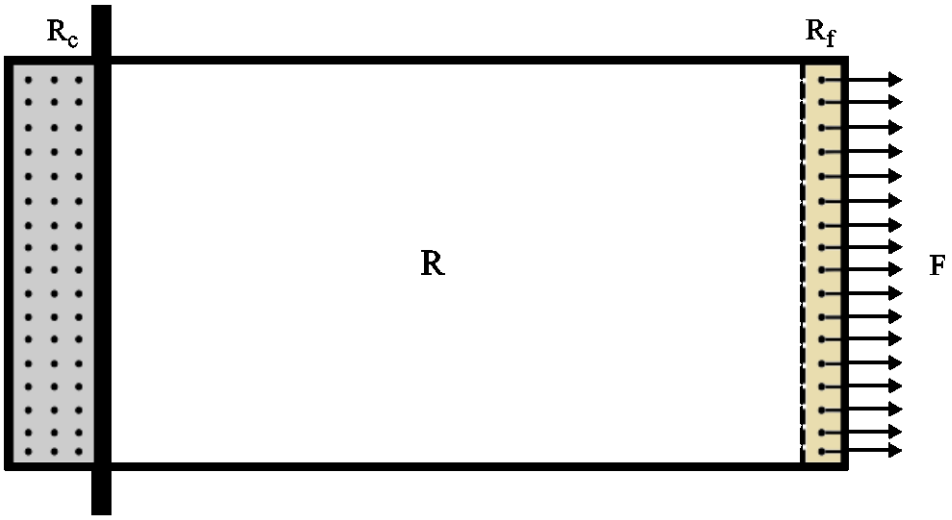


Figure 2: Regions $R_f$(Real) and $R_c$(imaginary) for loading application and boundary conditions.

## 2.5 Constrain Conditions

The integro-differential PD equation of motion contains spatial integrals and time derivatives in order to permit discontinuities. In PD, constrain conditions are used to represent boundary conditions. These conditions are applied on the displacement and velocity fields of an "extended imaginary material layer" $R_c$ along the boundary of a material region as shown in Figure 2. According to [2], this region is extended with the size of the horizon off the boundary.

## 2.6 External Loading

External loads in PD are applied as body forces. In the CCM theory, surface traction do appear unlike in PD. By applying an external load on a region, and divide that region into two domains, $\Omega^-$ and $\Omega^+$, one domain will exert force on the other, making it easy to find the force , $F^+$, by integrating the surface traction over the cross-sectional area of the domains, $\partial\Omega$, as

$$F^+ = \int_{\partial\Omega} T^s dA, \tag{17}$$

where $T^s$is the surface traction appearing on one of the domains. In the PD theory, using the last assumption, surface traction does not appear, but, force densities do appear when

material points from a domain interact with material points in the other domain. Therefore, by volume integrating the force densities over one of the domains, the force is found as

$$\mathrm{F}^{+} = \int_{\Omega+} \mathrm{M}(\mathrm{x})\mathrm{dV}, \tag{18}$$

while M is

$$\mathrm{M}(\mathrm{x}) = \int_{\Omega-} \big(\mathrm{t}(\mathrm{u}' - \mathrm{u}, \mathrm{x}' - \mathrm{x}) - \mathrm{t}'(\mathrm{u} - \mathrm{u}', \mathrm{x} - \mathrm{x}')\big)\mathrm{dV}. \tag{19}$$

Unlike CCM, in PD, one can note that the calculation of the force requires integration over domain $\Omega^{+}$, and M requires integration over domain $\Omega^{-}$. Consequently, if $\Omega^{-}$ disappears, the last integration of the force densities disappear. Correspondingly, body forces are applied on material points within the region, $\mathrm{R}_f$ as

$$\mathrm{b}(\mathrm{x}, \mathrm{t}) = -\frac{1}{\Delta}\mathrm{p}(\mathrm{x}, \mathrm{t})\mathrm{n} \tag{20}$$

and

$$\mathrm{b}(\mathrm{x}, \mathrm{t}) = \frac{1}{\mathrm{S}_l \Delta}\mathrm{P}(\mathrm{t}), \tag{21}$$

where $\mathrm{b}(\mathrm{x}, \mathrm{t})$ is the body force, $\mathrm{P}(\mathrm{t})$ is the point load and $\mathrm{p}(\mathrm{x}, \mathrm{t})$ is the distributed pressure.

## 2.7 Bond-Based PD

The principle of virtual work did fulfill the need of balancing both the linear momentum and energy in the PD equation of motion. In order to balance the angular momentum in the bond-based PD equation of motion, the force density vectors between any two interacting points have to be equal in magnitude and parallel to the deformed relative position vectors, expressed as

$$t(u' - u, x' - x) = T(x, t)\langle x' - x\rangle, = \frac{1}{2} C \frac{y' - y}{|y' - y|} = \frac{1}{2} f(u' - u, x' - x, t) \quad (22)$$

and

$$t'(u - u', x - x') = T(x', t)\langle x - x'\rangle = -\frac{1}{2} C \frac{y' - y}{|y' - y|} = -\frac{1}{2} f(u' - u, x' - x, t), \quad (23)$$

where "C is an unknown auxiliary parameter that depends on the engineering material constants, pairwise stretch between $x'$ and x, and the horizon"[7]. Therefore, the PD equation of motion can be rewriting as

$$\rho(x)\ddot{u}(x, t) = \int_H f(u' - u, x' - x)dH + b(x, t), \quad (24)$$

where $f(u' - u, x' - x)$ is the force density vector of the pairwise response function [38] which is defined as

$$f(u' - u, x' - x, t) = [c_0 s(u' - u, x' - x, t) - c_2 T] \frac{y' - y}{|y' - y|}, \quad (25)$$

where T is the ambient temperature at material points $x'$ and x. For a three-dimensional isotropic materials, the parameters $c_0$ and $c_2$ can be expressed as

$$c_0 = c = \frac{18k}{\pi\delta^4} \quad (26)$$

and

$$c_2 = c\alpha, \quad (27)$$

where k is the bulk modulus, α is the coefficient of thermal expansion and c is the bond function.

## 2.8 PD and CCM

A material point k can only interact with its nearest neighbors in all directions in the classical continuum mechanics theory. These interactions are denoted as "internal traction vectors", and are related to the Cauchy stress components as the following

$$\begin{Bmatrix} T_x \\ T_y \\ T_z \end{Bmatrix} = \begin{bmatrix} \sigma_{xx(k)} & \sigma_{xy(k)} & \sigma_{xz(k)} \\ \sigma_{xy(k)} & \sigma_{yy(k)} & \sigma_{yz(k)} \\ \sigma_{xz(k)} & \sigma_{yz(k)} & \sigma_{zz(k)} \end{bmatrix} \begin{Bmatrix} n_x \\ n_y \\ n_z \end{Bmatrix}. \tag{28}$$

When comparing the equation of motion of CCM and PD, the components of the strain energy density in each theory differs, stresses in CCM and micropotentials in PD. Considering local interactions in PD, the strain energy density is represented as

$$W_{(k)} = \frac{1}{2} \sum_{j=k+l,k-l,k+m,k-m,k+n,k-n} \frac{1}{2} (w_{(k)(j)}(y_{(1k)} - y_{(k)}, y_{(2k)} - y_{(k)}, \dots) + w_{(j)(k)}(y_{(1j)} - y_{(j)}, y_{(2j)} - y_{(j)}, \dots)) V_{(j)}, \tag{29}$$

where (l,m,n) represent the grid size in (x,y,z) directions. The PD equation of motion considering the same local interactions is defined as

$$\rho(x)\ddot{u}(x,t) = \sum_{j=k+1,k-1,k+m,k-m,k+n,k-n} (t_{(k)(j)} - t_{(j)(k)})V_{(j)} + b_{(k)}, \tag{30}$$

where

$$t_{(k)(j)} = \frac{1}{2} \frac{\partial w_{(k)(j)}}{\partial (y_{(j)} - y_{(k)})} \tag{31}$$

and

$$t_{(j)(k)} = \frac{1}{2} \frac{\partial w_{(j)(k)}}{\partial (y_{(k)} - y_{(j)})}. \tag{32}$$

Based on CCM, stress components can represent the equation of motion as

$$\rho(x)\ddot{u}(x,t) = \sigma_{\alpha x,x(k)} + \sigma_{\alpha y,y(k)} + \sigma_{\alpha z,z(k)} + b_{\alpha(k)}, \tag{33}$$

where α =(x,y,z). A relation between the Cauchy stresses and PD forces is obtained by using forward and back formulae of the finite difference approximation on equation 33, and equating the resultant expressions the resultant expression to equation 30. Stress components in terms of PD force densities are expressed as

$$\sum_{\beta=x,y,z} \sigma^2_{\alpha\beta(k)} = 4\left(t_{(k)(q_\alpha)}\left|x_{(q_\alpha)} - x_{(k)}\right|V_{(q_\alpha)}\right).\left(t_{(k)(q_\alpha)}\left|x_{(q_\alpha)} - x_{(k)}\right|V_{(q_\alpha)}\right). \tag{34}$$

Based on CCM, the strain energy density can be written as

$$W_{(k)} = \frac{k}{2}(\theta_k - 3\alpha T_{(k)})^2 + \left[\frac{1}{4\mu}\left(\sigma^2_{xx(k)} + \sigma^2_{yy(k)} + \sigma^2_{zz(k)}\right) + \frac{1}{4\mu}\left(\sigma^2_{xy(k)} + \sigma^2_{xz(k)} + \sigma^2_{yz(k)}\right) - \frac{3k^2}{4\mu}\theta^2_{(k)}\right], \tag{35}$$

where $\theta_{(k)}$ is the averaged value of the volumetric strain "dilatation", $T_{(k)}$ is the temperature change, α is the coefficient of thermal expansion, and k is the bulk modulus for isotropic material. By substituting stress components with PD force densities using the stress to force density relation from equation 34, the strain energy density is rewritten as

$$W_{(k)} = \frac{1}{2\mu}\sum_{j=k+1,k-1,k+m,k-m,k+n,k-n}\left(t_{(k)(q_\alpha)}\left|x_{(q_\alpha)} - x_{(k)}\right|V_{(q_\alpha)}\right).\left(t_{(k)(q_\alpha)}\left|x_{(q_\alpha)} - x_{(k)}\right|V_{(q_\alpha)}\right) + \frac{k}{2}(\theta_k - 3\alpha T_{(k)})^2 - \frac{3k^2}{4\mu}\theta^2_{(k)}. \tag{36}$$

After simplifying, a general form of the strain energy density for bond-based PD is expressed as

$$W_{(k)} = a\theta_{(k)}^2 - a_2\theta_k T_{(k)} + a_3 T_{(k)}^2 + \sum_{j=k+1,k-1,k+m,k-m,k+n,k-n} b_c(((|y_{(j)} - y_{(k)}| - |x_{(j)} - x_{(k)}|) - \alpha T_{(k)}|x_{(j)} - x_{(k)}|)^2 V_{(j)}), \quad (37)$$

where a, $a_2$, $a_3$, and $b_c$ are PD parameters.

## 2.9 Material parameters

The strain energy density for an isotropic nonlocal PD model is generalized to be

$$W_{(k)} = a\theta_{(k)}^2 - a_2\theta_k T_{(k)} + a_3 T_{(k)}^2 + b_c \sum_{j=1}^{N} w_{(k)(j)}(((|y_{(j)} - y_{(k)}| - |x_{(j)} - x_{(k)}|) - \alpha T_{(k)}|x_{(j)} - x_{(k)}|)^2 V_{(j)}), \quad (38)$$

where N is the number of family members and $V_{(j)}$ is the volume of material point j. The relation between the strain energy density and the force density vector is expressed as

$$t_{(k)(j)}(u_{(j)} - u_{(k)}, x_{(j)} - x_{(k)}, t) = \frac{1}{V_{(j)}} \frac{\partial W(x)}{\partial(|y_{(j)} - y_{(k)}|)} \frac{(y_{(j)} - y_{(k)})}{|y_{(j)} - y_{(k)}|}. \quad (39)$$

Considering that the dilatation and its associated terms disappear from the strain energy density expression in bond-based PD, the auxiliary parameter C from equations 22 and 23 becomes

$$C = 4b_c w_{(k)(j)} \left((|y_{(j)} - y_{(k)}| - |x_{(j)} - x_{(k)}|) - aT_{(k)}|x_{(j)} - x_{(k)}|\right). \quad (40)$$

By substituting the parameter value into the force density vector can be rewritten as

$$\mathrm{t}_{(k)(j)} = 2\mathrm{b_c} w_{(\mathrm{k})(j)} \Big( \big( \big|\mathrm{y}_{(j)} - \mathrm{y}_{(k)}\big| - \big|\mathrm{x}_{(j)} - \mathrm{x}_{(k)}\big| \big) - aT_{(k)} \big|\mathrm{x}_{(j)} - \mathrm{x}_{(k)}\big| \Big) \frac{(\mathrm{y}_{(j)} - \mathrm{y}_{(k)})}{\big|\mathrm{y}_{(j)} - \mathrm{y}_{(k)}\big|} \tag{41}$$

and

$$\mathrm{f}_{(k)(j)} = 4\mathrm{b_c} w_{(\mathrm{k})(j)} \big|\mathrm{x}_{(j)} - \mathrm{x}_{(k)}\big| \big(\mathrm{s}_{(k)(j)} - aT_{(k)}\big) \frac{\big(\mathrm{y}_{(j)} - \mathrm{y}_{(k)}\big)}{\big|\mathrm{y}_{(j)} - \mathrm{y}_{(k)}\big|}. \tag{42}$$

Comparing the last equation to equation 25, the influence function, $w_{(\mathrm{k})(j)}$, is expressed as

$$w_{(\mathrm{k})(j)} = \frac{\mathrm{c}}{4\mathrm{b_c}} \frac{1}{\big|\mathrm{x}_{(j)} - \mathrm{x}_{(k)}\big|}. \tag{43}$$

To include the effect of all family members, the influence function can be rewritten as

$$w_{(\mathrm{k})(j)} = \frac{\delta}{\big|\mathrm{x}_{(j)} - \mathrm{x}_{(k)}\big|}, \tag{44}$$

as the ratio of c/b has a dimension of length

$$\frac{\mathrm{c}}{\mathrm{b_c}} = 4\,\delta. \tag{45}$$

Substituting the influence function given in equation 44 to equation 41, a final force density vector form is given as

$$\mathrm{t}_{(k)(j)} = 2\delta \big\{ \mathrm{b_c} (\mathrm{s}_{(k)(j)} - aT_{(k)}) \big\} \frac{(\mathrm{y}_{(j)} - \mathrm{y}_{(k)})}{\big|\mathrm{y}_{(j)} - \mathrm{y}_{(k)}\big|}. \tag{46}$$

Furthermore, for bond-based PD, the parameter b is obtained after equating both the expressions of the strain energy density in the realm of CCM and the evaluated PD strain energy density for a simple shear case for two-dimensional structures as

$$b_c = \frac{6\mu}{\pi h \delta^4}, \tag{47}$$

where h represents the thickness, μ is the shear modulus $\mu = E/2(1+v)$, Poisson's ratio $v$ = 1/3, the bulk modulus as $k = 2\mu$,

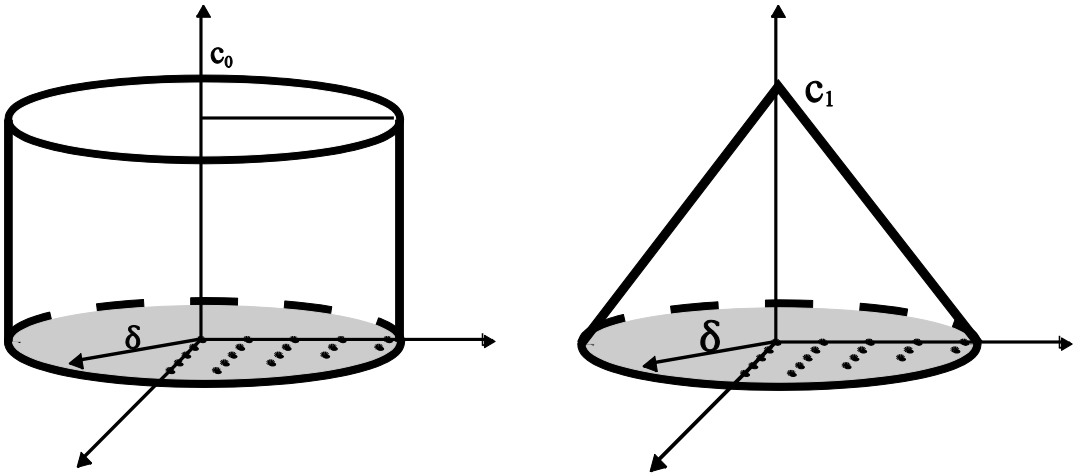


Figure 3: different bond function effects within a horizon (left) conical (right) constant.

For FGMs, the modulus of elasticity, E, used in PD parameter b will represent the average modulus of elasticity of two interacting points [52], in the form

$$E = \frac{E_k + E_j}{2}. \tag{48}$$

As shown in Figure 3, a constant bond function, $c_0$, for two-dimensional models will contain is

$$c_0 = \frac{6E}{\pi h \delta^3 (1-v)}. \tag{49}$$

To provide PD convergence to the local solutions, one can use a conical bond function,$c_1$, expressed as

$$c_1 = \frac{24E}{\pi h \delta^3 (1-v)} \left(1 - \frac{\boldsymbol{x_j} - \boldsymbol{x_k}}{\delta}\right). \tag{50}$$

## 2.10 Surface Correction

Although this section is not implemented in this work, surface correction could improve the PD results. Due to the dependency of the PD parameter b on the horizon integration, this parameter needs to be corrected if the horizon of a material point is not fully embedded in the material region or if located on an interface of two different materials. The correction can be achieved by comparing both the strain energy density of a point in PD and the strain energy density of a point in CCM for a uniaxial stretch loading condition. The resulting displacement field from the constant displacement gradient $\frac{\partial \mathrm{u}_{\alpha}^{*}}{\partial \alpha}\alpha = \zeta$, with $\alpha = x, y, z$ is given as

$$\mathrm{U}_1^T(x) = \left\{\frac{\partial \mathrm{u}_{\mathrm{x}}^{*}}{\partial \mathrm{x}} x \; 0 \quad 0\right\}, \tag{51}$$

$$\mathrm{U}_2^T(x) = \left\{0 \; \frac{\partial \mathrm{u}_{\mathrm{y}}^{*}}{\partial \mathrm{y}} y \quad 0\right\}, \tag{52}$$

$$\mathrm{U}_3^T(x) = \left\{0 \quad 0 \quad \frac{\partial \mathrm{u}_{\mathrm{z}}^{*}}{\partial \mathrm{z}} z\right\}. \tag{53}$$

The strain energy density terms for PD and CCM, respectively, are expressed as

$$\mathrm{W}_{\mathrm{m}}^{PD}\left(\mathrm{x}_{(k)}\right) = \delta \, \mathrm{b}_{\mathrm{c}} \sum_{\mathrm{j}=1}^{N} \frac{1}{\left|\mathrm{x}_{(j)} - \mathrm{x}_{(k)}\right|}\left(\left|\mathrm{y}_{(j)} - \mathrm{y}_{(k)}\right| - \left|\mathrm{x}_{(j)} - \mathrm{x}_{(k)}\right|\right)^2 \mathrm{V}_{(\mathrm{j})} \tag{54}$$

and

$$\mathrm{W}_{\mathrm{m}}^{CM}\left(\mathrm{x}_{(k)}\right) = \frac{1}{2}\zeta^2 \mu \tag{55}$$

where m = 1,2,3 representing the three coordinates. The parameter b correction term is

$$S_{m(k)} = \frac{W_m^{CM}(x_{(k)})}{W_m^{PD}(x_{(k)})} = \frac{\frac{1}{2}\zeta^2\mu}{\delta\, b_c \sum_{j=1}^{N} \frac{1}{|x_{(j)}-x_{(k)}|}\left(|y_{(j)}-y_{(k)}| - |x_{(j)}-x_{(k)}|\right)^2 V_{(j)}}. \quad (56)$$

Vectors of the correction factors for points k and j can be written as

$$g_{(b_c)(k)}(x_{(k)}) = \{g_{x(b_c)(k)}, g_{y(b_c)(k)}, g_{z(b_c)(k)}\}^T = \{S_{1(k)}, S_{2(k)}, S_{3(k)}\}^T \quad (57)$$

$$g_{(b_c)(j)}(x_{(j)}) = \{g_{x(b_c)(j)}, g_{y(b)(j)}, g_{z(b_c)(j)}\}^T = \{S_{1(j)}, S_{2(j)}, S_{3(j)}\}^T. \quad (58)$$

The correction factor for an interaction between the two points using the principle values of an ellipsoid is given as

$$g_{(b)(k)(j)} = \{g_{x(b_c)(k)(j)}, g_{y(b_c)(k)(j)}, g_{z(b_c)(k)(j)}\}^T = \frac{g_{(b)(k)} + g_{(b)(j)}}{2}. \quad (59)$$

Hence, the correction factor obtained after intersecting the ellipsoid with the relative position vector $n = (x_{(j)} - x_{(k)})/|x_{(j)} - x_{(k)}|$ is

$$G_{(b)(k)(j)} = ([n_x/g_{x(b)(k)(j)}]^2 + [n_y/g_{y(b)(k)(j)}]^2 + [n_z/g_{z(b)(k)(j)}]^2)^{-1/2}. \quad (60)$$

One can express the corrected form of the strain energy density as

$$W_{(k)} = \delta\, b_c \sum_{j=1}^{N} G_{(b_c)(k)(j)} \frac{1}{|x_{(j)} - x_{(k)}|}\left(|y_{(j)} - y_{(k)}| - |x_{(j)} - x_{(k)}|\right)^2 V_{(j)}. \quad (61)$$

## 2.11 Volume correction

In PD, the full volume of all points within the horizon of the point of interest is assumed. Some points are not fully covered within the horizon require volume approximations. Therefore, points within the range $\xi_{(k)(j)} = |x_{(j)} - x_{(k)}| > \delta - r$, where $r = \Delta/2$, will require a volume correction factor of $v_{c(j)} = (\delta + r - \xi_{(k)(j)})/2r$.

## 2.12 Time integration

The acceleration of a point can be calculated from the PD equation of motion. The PD equation of motion in the time step form for a horizon size $\delta = 2\Delta$ is written as

$$\begin{aligned}\rho_{(k)}\ddot{u}_{(k)} = (t^{n}_{(k)(k+1)} & \\ - t^{n}_{(k+1)(k)})(v_{c(k+1)}V_{(k+1)}) + (t^{n}_{(k)(k+2)} & \\ - t^{n}_{(k+2)(k)})(v_{c(k+2)}V_{(k+2)}) + (t^{n}_{(k)(k-1)} & \\ - t^{n}_{(k-1)(k)})(v_{c(k-1)}V_{(k-1)}) + (t^{n}_{(k)(k-2)} & \\ - t^{n}_{(k-2)(k)})(v_{c(k-2)}V_{(k-2)}) + b^{n}_{(k)}. &\end{aligned} \tag{62}$$

The force density vector in the time step form can be written as

$$t^{n}_{(j)(k)} = \frac{\xi_{(k)(j)} + \eta^{n}_{(j)(k)}}{\left|\xi_{(k)(j)} + \eta^{n}_{(j)(k)}\right|}\left(2b_c \delta s^{n}_{(j)(k)}\right) \tag{63}$$

and

$$t^{n}_{(k)(j)} = -\frac{\xi_{(k)(j)} + \eta^{n}_{(j)(k)}}{\left|\xi_{(k)(j)} + \eta^{n}_{(j)(k)}\right|}\left(2b_c \delta s^{n}_{(k)(j)}\right), \tag{64}$$

where

$$\xi_{(k)(j)} = x_{(j)} - x_{(k)} \tag{65}$$

and

$$\eta^{n}_{(j)(k)} = u^{n}_{(j)} - u^{n}_{(k)} \tag{66}$$

The stretch in the time step form can be written as

$$s^{n}_{(k)(j)} = \frac{\left|\xi_{(k)(j)} + \eta^{n}_{(j)(k)}\right| - \left|\xi_{(k)(j)}\right|}{\left|\xi_{(k)(j)}\right|}. \tag{67}$$

The velocity and the displacement of a point in the next time step can be calculated using

$$\dot{u}_{(k)}^{n+1} = \ddot{u}_{(k)}\,\Delta t + \dot{u}_{(k)}^{n} \tag{68}$$

and

$$u_{(k)}^{n+1} = \dot{u}_{(k)}^{n+1}\,\Delta t + u_{(k)}^{n}. \tag{69}$$

## 2.13 Time step

In PD, a stability condition is considered by calculating the time step size, $\Delta t$, multiplied to a factor of safety less than one to obtain convergent results. Time step size can be calculated according to

$$\Delta t < \sqrt{\frac{2\rho_{(k)}}{\sum_j \left(\frac{4b_c\delta}{|\xi_{(k)(j)}|}\right)(v_{c(j)}V_{(j)})}}. \tag{70}$$

When using the adaptive dynamic relaxation, it is recommended to use a time step size $\Delta t = 1$.

## 2.14 Adaptive Dynamic Relaxation (ADR)

ADR technique was first introduced in [107]. This technique can be implemented in PD models to solve static problems and reach the steady state by determining the damping coefficient every time step. In ADR, differential equations can represent the PD equation of motion in the form

$$D\ddot{U}(X,t) + c_d D\dot{U}(X,t) = F(U,U',X,X'), \tag{71}$$

where D is the fictitious diagonal density matrix, $c_d$ is the damping coefficient, X is the initial positions, U is the displacements and F is a vector that contains the force density vector pairwise function and the body force, given as

$$\mathrm{X}^{T} = \left\{\mathrm{x}_{(1)}, \mathrm{x}_{(2)}, \dots, \mathrm{x}_{(M)}\right\} \tag{72}$$

and

$$\mathrm{U}^{T} = \left\{\mathrm{u}\left(\mathrm{x}_{(1)}, \mathrm{t}\right), \mathrm{u}\left(\mathrm{x}_{(2)}, \mathrm{t}\right), \dots, \mathrm{u}\left(\mathrm{x}_{(\mathrm{M})}, \mathrm{t}\right)\right\} \tag{73}$$

$$\mathrm{F}_{(\mathrm{k})} = \sum_{\mathrm{i}=1}^{\mathrm{N}} \left(\mathrm{t}_{(k)(j)} - \mathrm{t}_{(k)(j)}\right) \left(\mathrm{v}_{c(j)} \mathrm{V}_{(\mathrm{j})}\right) + \mathrm{b}_{(k)}. \tag{74}$$

To calculate the velocity in the time step form, one can use the central-difference explicit integration. For the first time step, the displacement is zero and the velocity is given as

$$\dot{\boldsymbol{U}}^{\mathbf{1/2}} = \frac{\mathbf{\Delta t D^{-1} F^{0}}}{\mathbf{2}} \tag{75}$$

while the displacement and the velocity for the next time steps are expressed as

$$\dot{U}^{n+1/2} = \frac{\left((2 - c^{n}\Delta \mathrm{t})\dot{U}^{n-1/2} + 2\Delta \mathrm{t D^{-1}} \mathrm{F}^{n}\right)}{\left(2 + c_{d}^{n}\Delta \mathrm{t}\right)} \tag{76}$$

and

$$\mathrm{U}^{n+1} = \mathrm{U}^{n} + \Delta \mathrm{t}\dot{U}^{n+1/2}. \tag{77}$$

Based on Greschgorin's theorem, the fictitious diagonal elements of the density matrix, D, are given as

$$\lambda_{ii} \geq \frac{1}{4}\Delta \mathrm{t}^{2} \sum_{j} \left|K_{ij}\right| \tag{78}$$

where $K_{ij}$ is the stiffness matrix of the system. The damping coefficient can be obtained from the first equation in the time step form, given as

$$\ddot{\mathrm{U}}^{n}(\mathrm{X}, \mathrm{t}^{n}) + c_{d}^{n}\dot{U}^{n}(\mathrm{X}, \mathrm{t}^{n}) = \mathrm{D}^{-1}\mathrm{F}^{n}(\mathrm{U}^{n}, U'^{n}, X, X'), \tag{79}$$

as

$$c_d^n = 2\sqrt{\frac{((\mathrm{U}^n)^T\ {}^1K^n\mathrm{U}^n}{(\mathrm{U}^n)^T\mathrm{U}^n}}, \tag{80}$$

where ${}^1K^n$ is the diagonal stiffness matrix, given as

$${}^1K_{ii}^n = -(F_i^n/\lambda_{ii} - F_i^{n-1}/\lambda_{ii})/(\Delta t\dot{u}_i^{n-1/2}). \tag{81}$$

## 2.15 Numerical Convergence

The choice of the grid size, Δ, and the horizon size, δ, in PD is important in order to obtain accurate solutions. The criteria of choosing the size of the horizon in PD rely on the length scale used in the model. For macroscale models, horizon sizes of $\delta = \Delta$ and $3\Delta$ were found to provide accurate results, note that, $\delta = \Delta$ represent local interactions. For nanoscale, it is better to assign a horizon size equal to the maximum natural interaction distance between atoms.

## 2.16 Memory Limitation

As there could be a huge number of material points within a PD model, storing the family members for each material point will be a challenge. A technique suggests the creation of a storing system that consist of two separate arrays to overcome this limitation. One array contains all stored family members, while the second contains first array's information. Each row in the second array indicates a row number from the first array which in turn indicates the location of family members of each material point.

# 3 NON-GRADIENT TOPOLOGY OPTIMIZATION

Topology optimization is a relatively new but rapidly expanding research field, which has potential applications in the aerospace manufacturing industry. Starting with the landmark paper of Bendsoe and Kikuchi [78], numerical methods for topology optimization have been investigated extensively since the late 1980s. Here, an efficient and simple non-gradient heuristic PTO approach adopted from [97] is implemented in this work. This chapter presents the theory behind the full optimization process in three sections. Section 3.1 discusses the optimization approach in terms of the problem, the function and the material model; Section 3.2 presents the projection operator and the optimization stopping criteria; and Section 3.3 explains the optimization algorithm.

## 3.1 Proportional Topology Optimization (PTO)

### 3.1.1 Minimum Strain Energy Density Problem

To demonstrate the topology optimization problem of this study, a material volume constraint is considered with a density design variable, while minimizing the PD strain energy density as the objective function. This problem can be written as follows:

$$\begin{cases} \min W \\ \text{such that } \begin{cases} \sum_{k=1}^{N} \varphi_k V_k = \overline{V}, \\ 0 \le \varphi_k \le 1 \end{cases} \end{cases} \tag{82}$$

where W is the PD strain energy density, $V_k$ is the volume of material point k, $\varphi_k$ is the density of material point k, $\overline{V}$ is the volume constraint or volume fraction and N is the total number of material points.

### 3.1.2 Material Model

The material property of each PD material point in the PTO method is set based on a modified SIMP approach in [85, 86] as

$$E(\varphi_k) = E_{min} + \varphi_k^{P_n}(E_0 - E_{min}), \quad (83)$$

where E is a density dependent modulus of elasticity for the material point k, $E_0$ and $E_{min}$ are the modulus of elasticity for the solid material region and the modulus of elasticity for the void material region, respectively and $P_n$ is the penalization coefficient used to reduce gray material zones. In this study, the elastic modules for both the solid and void material regions are $10^7$GPa and $10^4$GPa, respectively.

### 3.1.3 Density Distribution

The minimization of the PD strain energy density is the objective function of this optimization problem, and considering that a design variable can be either discrete or continuous, [106] reported that continuous design variables are more desirable than discrete design variables for the purpose of the minimization of the objective function in topology optimization methods. In PTO, continuous design variables are employed. The continuous design variable approach permits the design variable to have any varying value between 0 and 1. However, in the discrete design variable approach, the design variable can only be assigned a value of either 0 or 1 to represent void or solid material regions, respectively. For initialization purposes, the optimization problem begins with an assigned value of density equal to 0.5 distributed among all the material points within the structure. Following as the first step, a strain energy density dependent density is calculated for each material point within the structure using

$$\varphi_k^{opt} = \frac{RM}{\sum_{j=1}^{N} W_j^q V_j} W_k^q, \quad (84)$$

where $\varphi_k^{opt}$ is the optimal particle density in the current iteration for material point k, RM is the remaining material amount, $(j = 1,2,..,N)$ represents the number of material points and q is the proportion exponent equal to 1. The density of each material point passing to the next optimization iteration is calculated based on

$$\varphi_k^{new} = \vartheta\varphi_k^{prev} + (1 - \vartheta)\varphi_k^{opt}, \quad (85)$$

where $\varphi_k^{new}$ is the density of point k passing to the next iteration, $\varphi_k^{prev}$ is the density of point k in the last iteration and $\vartheta$ is the history coefficient set as 0.5. The history coefficient is a dimensionless factor that creates a dependency relation for next iteration's density on the current and previous densities.

### 3.1.4 Density Filtering

Filtering has several advantages, one of the most significant advantages considered in this study is the prevention of the checkerboard phenomena. The density of each material point is filtered in accordance to its neighboring material points within the filter radius R. Although, the checkerboard phenomena possess high stiffness, it is artificial [108]. The filtered density of material point k, $\widehat{\varphi}_k$, is defined as

$$\widehat{\varphi}_k = \frac{\left(\sum_{j=1}^{N_f} \gamma_{kj} \varphi_j^{opt}\right)}{\sum_{j=1}^{N_f} \gamma_{kj}}, \tag{86}$$

where $(j = 1,2,..,N_f)$ represents the number of material points within the filter radius of material point k and $\gamma_{kj}$ is a filter weight given as

$$\gamma_{kj} = R - |x_k - x_j|. \tag{87}$$

## 3.2 Projection Operator

### 3.2.1 Heaviside-type projection operator

As mentioned earlier, a material point that reaches a density value equal or close to the upper density limit represent a solid material point, vice versa. However, when material points reach neither the upper limit nor the lower limit, nor close to any, a material region called "gray material region" develop. Note that a gray material region is neither a solid nor a void material region. This material region is a result for uncertain topological details. To obtain a distinct optimal topology and to alter any non-distinct values into discrete, a Heaviside-type projection operator is employed as [109]

$$A_k = 1 - \frac{\varphi_k^{new}}{\eta}, \tag{88}$$

$$B_k = \frac{\varphi_k^{new} - \eta}{1 - \eta}, \tag{89}$$

$$\varphi_k^{new} = \begin{cases} \eta[\exp(-\beta A_k) - A_k \exp(-\beta)] & \text{if } 0 < \varphi_k^{new} \leq \eta \\ (1-\eta)[1 - \exp(-\beta B_k) + B_k \exp(-\beta)] + \eta & \text{if } \eta < \varphi_k^{new} \leq 1 \end{cases}, \tag{90}$$

where $\eta$ is a projection parameters that is equal to 0.5 and $\beta$ is a projection parameter defined in a continuation projection scheme.

### 3.2.2 Discreteness

When a projection operator is employed, the stop criterion for the optimization process is the discreteness which is according to [109], given as

$$D_t = \frac{\sum_{k=1}^{N} 4\,\varphi_k^{new}(1 - \varphi_k^{new})}{N} \times 100\%. \tag{91}$$

At the beginning of the optimization process when all material points are initialized with a density value of 0.5 the discreteness is 100%. As the name suggests, an optimal topology is fully discrete when reaching a discreteness of 0%.

## 3.3 The Optimization Algorithm

The algorithm of the proportional topology optimization based on PD is shown in Algorithm 1. To begin, PD analysis is performed until its stop criterion is satisfied; the strain energy density for each material point is calculated and exported to the optimization algorithm; the remaining material amount is set to be equal to the target material amount, given as

$$\text{Target Materil Amount} = \text{Number of material points} \times \overline{V}.$$

Remaining material is then distributed among all material points based on the strain energy density value and the density filter is applied. The actual material amount is calculated and the remaining material amount is updated as the following

$$\text{Remaining Material Amount} = \text{Target Material Amount} - \text{Actual Material Amount}.$$

Last but not least, the density is updated; the projection operator is employed; and the full process repeats until reaching convergence.

Algorithm 1: PTO

- Until convergence
    - Perform PD and calculate strain energy density of the structure
    - Check stop criteria, break if satisfied
    - Run optimization algorithm
        - Set remaining material amount
        - Until remaining material amount is small enough
        - Distribute remaining material amount to particles proportionally to their strain energy density values
        - Apply filter
        - Calculate actual material amount
        - Update remaining material amount
        - Update density
        - Apply projection operator

Algorithm 1: Pseudo code of the proportional topology optimization modified for the PD approach [97].

# 4 RESULTS AND DISCUSSION

This chapter presents seven case studies to illustrate the application of peridynamics in topology optimization. During the implementation of the case studies, the following aspects of the theoretical implementation are discussed:

- The volume constraint; the stopping criteria; the design space;
- The projection operator and its associated parameters;
- The computational cost; the stiffness of models; the optimal strain energy density;
- The conical and the constant PD bond functions; the various boundary conditions;
- Validation; the horizon size selection; the semi-checkerboard phenomena.

## 4.1 Case 1: 1:1 cantilever beam subjected to a point load at the middle of the free end

A cantilever beam is subjected to a point load at the middle of the free end is shown in Figure 4. The beam has a length to width ratio 1:1, a thickness of $\Delta$ and a boundary region extension of $\delta$. The elastic modules for the solid material region and the void material region is set to $10^7$GPa and $10^4$GPa, respectively. A Poisson's ratio v = 1/3 is used and a body force equal to $2\times10^{11}$ N/m$^3$ is applied. The ADR technique is employed with a time step size $\Delta t = 1$. A PD horizon size $\delta = 2\Delta$, a filter radius $R = 1.5\Delta$, a penalization coefficient of 3 and a material volume constraint of 50% is used. When the optimization begins, the design variable equal to 0.5 is set uniformly among all material points within the structure. Projection parameters $\eta$ and $\beta$ are given as 0.5 and 1.5, respectively. In this section, a 0.5 incremental increase of the projection parameters $\beta$ every 50 iteration is applied, otherwise, it is noted. Several models are discretized into uniformly distributed volumetric material points of $22 \times 22$, $66 \times 66$ and $100 \times 100$. A tolerance of 0.001 for the maximum change in particle densities between successive iterations is considered as the stopping criteria if the projection operator is not employed. On the other hand, if projection is employed, the optimization process is assumed to be converged when the discreteness. $D_t$, reaches 1%.

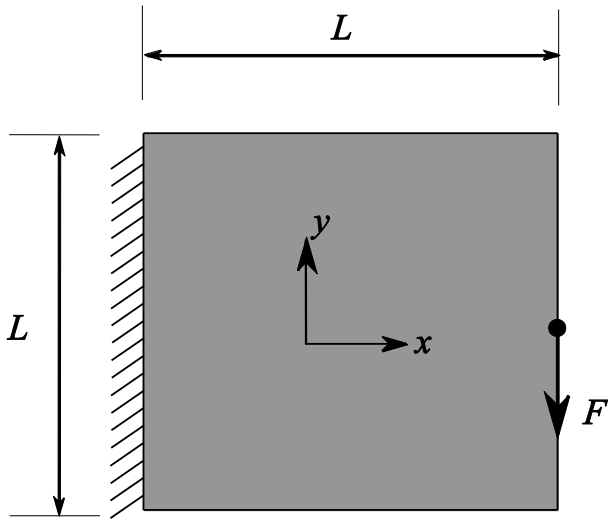


Figure 4: Geometry and loading for the 1:1 length to width ratio cantilever beam with a load at the middle of the free end.

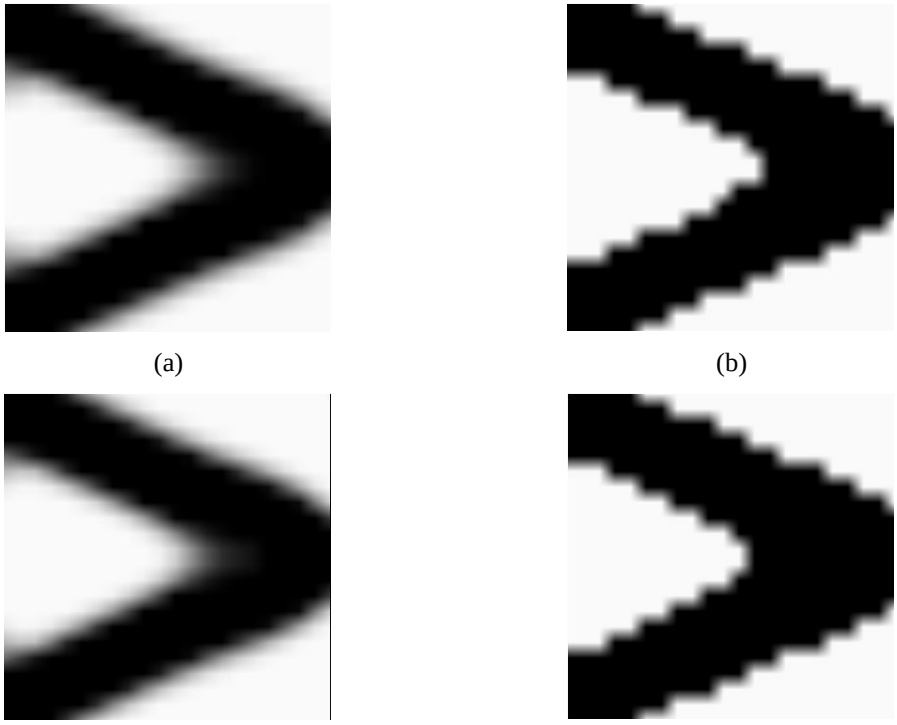

(a) (b)

(c) (d)

Figure 5: Optimal topologies for $22 \times 22$ material points with a horizon size $2\Delta$. (a) Without the conical bond function and the projection method (iteration 18). (b) Without the conical bond function and with the projection operator (iteration 252). (c) With the conical bond function and without the projection operator (iteration 21). (d) With the conical bond function and with the projection operator (iteration 252).

Comparing the results in Figure 5, one can note that the conical bond function does not affect the optimization process negatively. However, as mentioned in chapter 2, the conical bond function converges the PD results to the classical local theories. Moreover, one can clearly find that the projection operator improves the optimal topological results by eliminating the gray material zones. Note that there is a significant change on the number of iterations required to obtain the optimal topology when applying the projection operator. To study the dependency of the optimal topological results on the volume constraint, Figure 6 shows several optimal topologies for the $22 \times 22$ beam using various volume constraints. The conical bond function is employed while considering a 0.25 incremental increase of the projection parameters $\beta$ every 50 iteration.

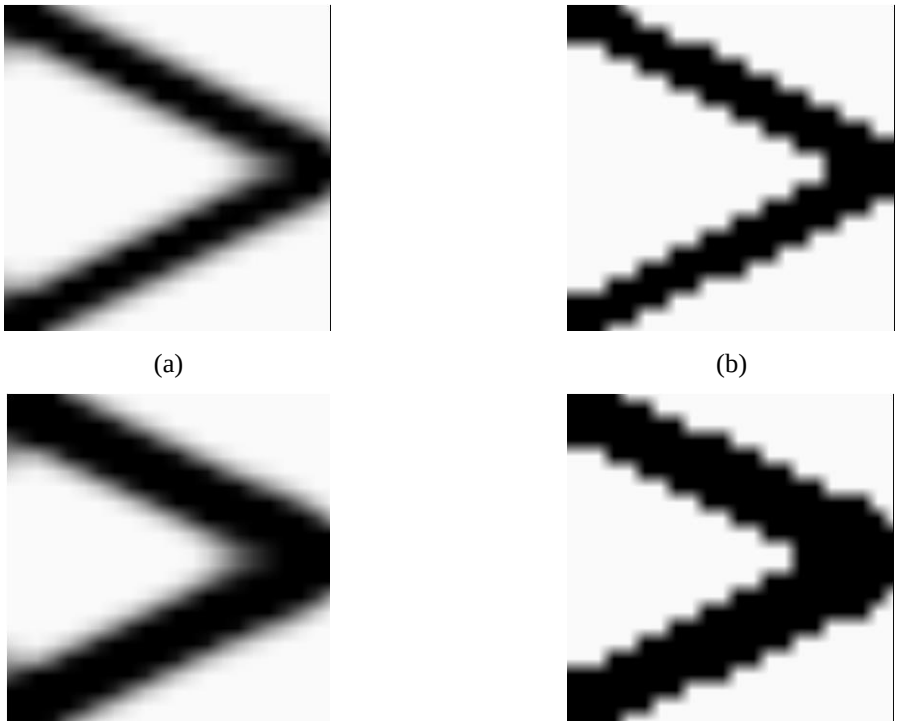

(a) (b)

(c) (d)

(e) (f)

(g) (h)

Figure 6: Optimal topologies with various volume constraints for $22 \times 22$ material points with a horizon size $2\Delta$ (a) 30% volume constraint (iteration 27). (b) 30% volume constraint (iteration 453) with the projection operator. (c) 40% volume constraint (iteration 21). (d) 40% volume constraint (iteration 402) with the projection operator. (e) 60% volume constraint (iteration 18). (f) 60% volume constraint (iteration 402) with the projection operator. (g) 70% volume constraint (iteration 39). (h) 70% volume constraint (iteration 402) with the projection operator.

From Figure 6, it is clear that the volume constraint influences the optimal topology. Increasing the volume constraint allows the generated topological model to utilize a greater number of material points to represent the solid material region, vice versa. To study the dependency of the optimal topological results on the number of material points, two additional models are discretized into uniformly distributed volumetric material points of $66 \times 66$ and $100 \times 100$ are presented.

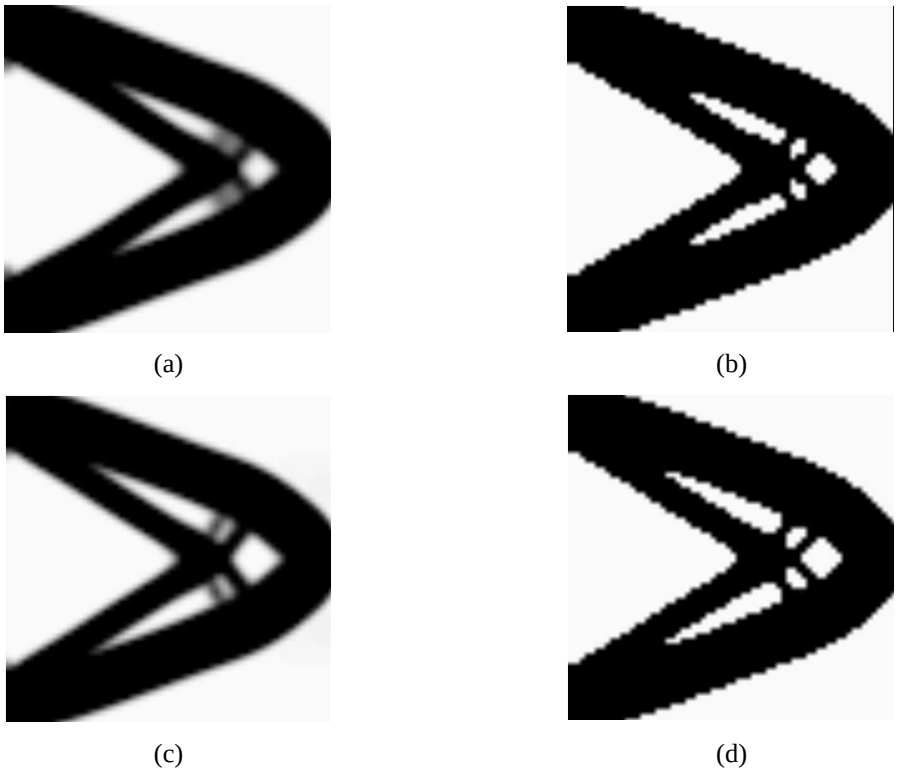

(a) (b)

(c) (d)

Figure 7: Optimal topologies for $66 \times 66$ material points with a horizon size $2\Delta$ with the conical bond function. (a) Without the conical bond function and the projection operator (iteration 30). (b) Without the conical bond function and with the projection operator (iteration 204). (c) With the conical bond function and without the projection operator (iteration 36). (d) With the conical bond function and with the projection operator (iteration 204).

Comparing the optimal topological results shown in Figure 7 for the $66 \times 66$ beam with the optimal topological results shown in Figure 5 for the $22 \times 22$ beam explain the relation between the obtainable optimal topology and the number of material points. To illustrate, one can clearly realize the development of the additional material regions around the center of the beam in the $66 \times 66$ example. Therefore, a greater number of material points within a domain represent a larger design space for the optimization, vice versa.

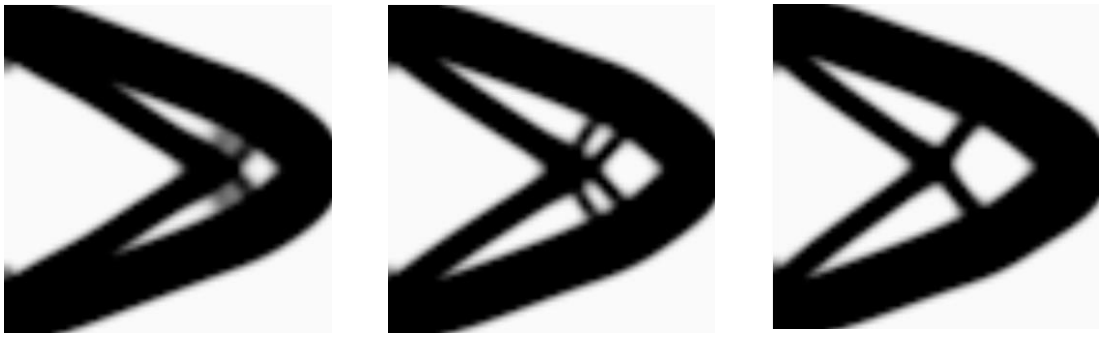

(a) (b) (c)

Figure 8: Optimal topologies for $66 \times 66$ material points with a horizon size $2\Delta$ and without the conical bond function considering various tolerances for the maximum change in particle densities between successive iteration. (a) With a tolerance of 0.001 for the maximum change in particle densities between successive iterations (iteration 30). (b) With a tolerance of $10^{-4}$ for the maximum change in particle densities between successive iterations (iteration 450). (c) With a tolerance of $10^{-5}$ for the maximum change in particle densities between successive iterations (iteration 2070).

As mentioned at the beginning of the section, if the projection operator is not employed, an assumed value of tolerance for the maximum change in particle densities between successive iterations is considered as the optimization stopping criteria. Figure 8 demonstrate the different optimal topological results obtained using various tolerance assumptions. By reducing the assigned tolerance value, one can clearly find that the number of iterations required to obtain an optimal topology is significantly increasing, vice versa. In addition, the optimal topological results differ from one and another, which may express the continuous topological development through the optimization iterations. Furthermore, the optimal topological results for the $100 \times 100$ model are shown in Figure 9.

(a)



(b)

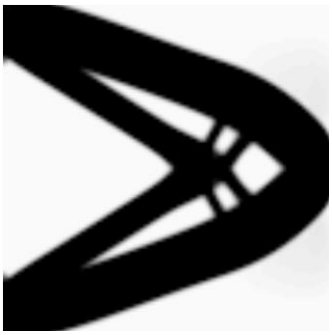

(c)

(d)

Figure 9: Optimal topologies for $100 \times 100$ material points with a horizon size $2\Delta$. (a) Without the conical bond function and the projection operator (iteration 42). (b) Without the conical bond function and with the projection operator (iteration 201). (c) With the conical bond function and without the projection operator (iteration 45). (d) With the conical bond function and with the projection operator (iteration 201).

In this model after examining Figure 9 and comparing all the optimal topological results, one may notice a difference between the optimal topologies being in the formation of additional material regions in some topological results than others. Such material regions only appear on the topologies obtained for the examples that employ the projection operator. Correspondingly, since the projection operator is only implemented to eliminate the gray areas, the fact that it could further affect the final result has to be considered. In order to solve this issue, the projection parameter $\beta$ should increase with smaller increments to give the topology enough time to develop. Likewise, the number of iterations between the sequence increases of the projection parameter $\beta$ should increase. To study the influence of the projection operator on the final topologies, Figure 10 presents the optimal topological results for the $100 \times 100$ beam when considering various random projection conditions.

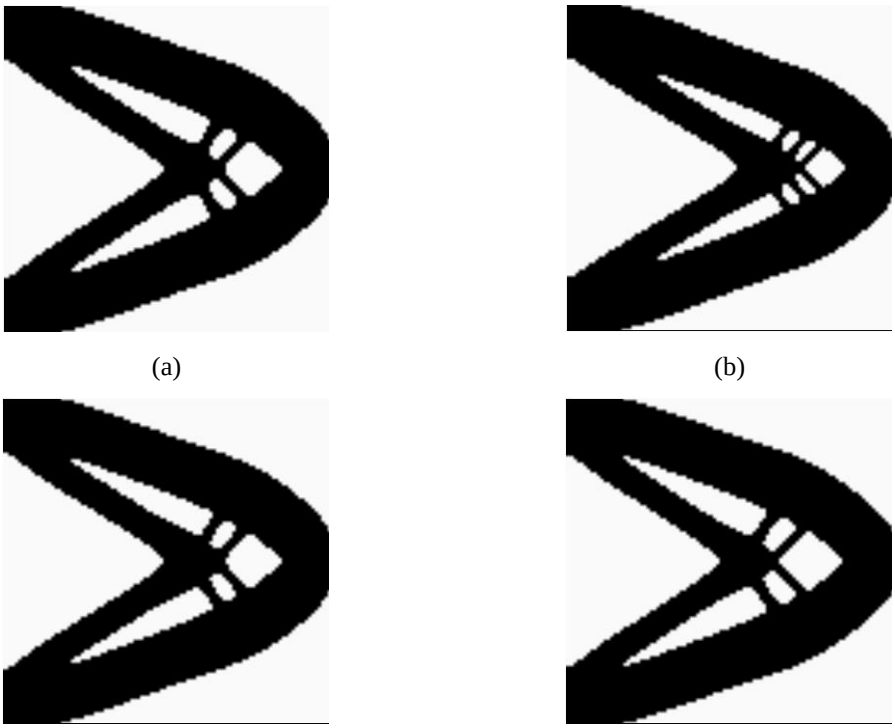

(a) (b)

(c) (d)

Figure 10: Optimal topologies for $100 \times 100$ material points with a horizon size $2\Delta$ and with the conical bond function under different projection conditions. (a) A projection parameter $\beta$ increase of 0.5 every 150 iteration. (b) A projection parameter $\beta$ increase of 0.5 every 50 iterations. (c) A projection parameter $\beta$ increase of 0.15 every 50 iterations. (d) A projection parameter $\beta$ increase of 0.15 every 150 iterations.

Four random projection conditions are tested and compared in Figure 10. The issue associated with the selection of the projection condition is proved to be solved by either using a smaller increments increase of the projection parameter $\beta$ or by increasing the number of iterations between the sequence increases of the projection parameter $\beta$ or both. The optimal topological results obtained using an increase of the projection parameter $\beta$ of 0.15 every 150 iterations, 0.15 every 50 iterations or 0.5 every 150 iterations are all acceptable. However, the number of iterations required to obtain an optimal topology differs from a projection condition to another. Therefore, the discreteness relation with the number of iterations required to obtain the optimal topologies for the previously discussed projection conditions is plotted in Figure 11.

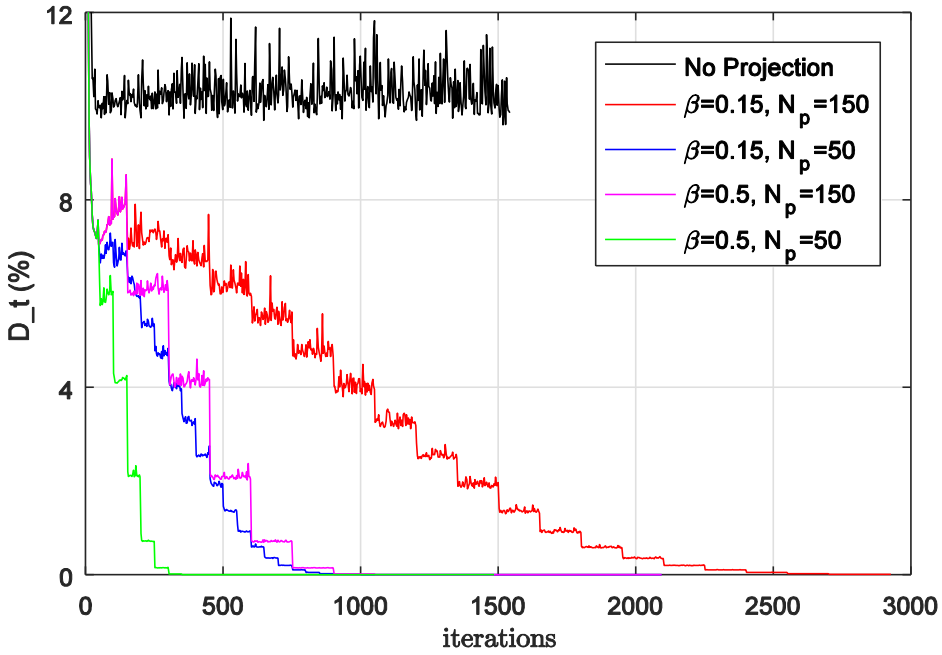


Figure 11: Discreteness of the different projection conditions ($N_p$ represents number of iteration between the sequence increases of the projection parameter $\beta$).

For further presentation of the advantages behind employing the projection operator, Figure 12 shows the optimal topological result for the $100 \times 100$ beam at 70% volume constraints. The conical bond function is employed while considering a 0.15 increment increase of the projection parameters $\beta$ every 100 iteration.

(a) (b)

Figure 12: Optimal topology at 70% volume constraints for $100 \times 100$ material points with a horizon size $2\Delta$ with the conical bond function. (a) Without the projection operator at 70% volume constraint (iteration 33). (b) With the projection operator with a projection parameter $\beta$ increase of 0.15 every 100 iterations at 70% volume constraint (iteration 1101).

As illustrated in Figure 12, one can find the huge improvements on the optimal topological results after the employment of the projection operator. However, the

difference between the numbers of iterations required to obtain the optimal topological result is significant. Another important factor that needs to be explored is the PD horizon size. To explain the selection criteria of the horizon size, Figure 13 shows the optimal topological results for a $100 \times 100$ material points beam using various horizon sizes. All examples employ the conical bond function while considering a 0.15 increment increase of the projection parameters $\beta$ every 150 iteration.

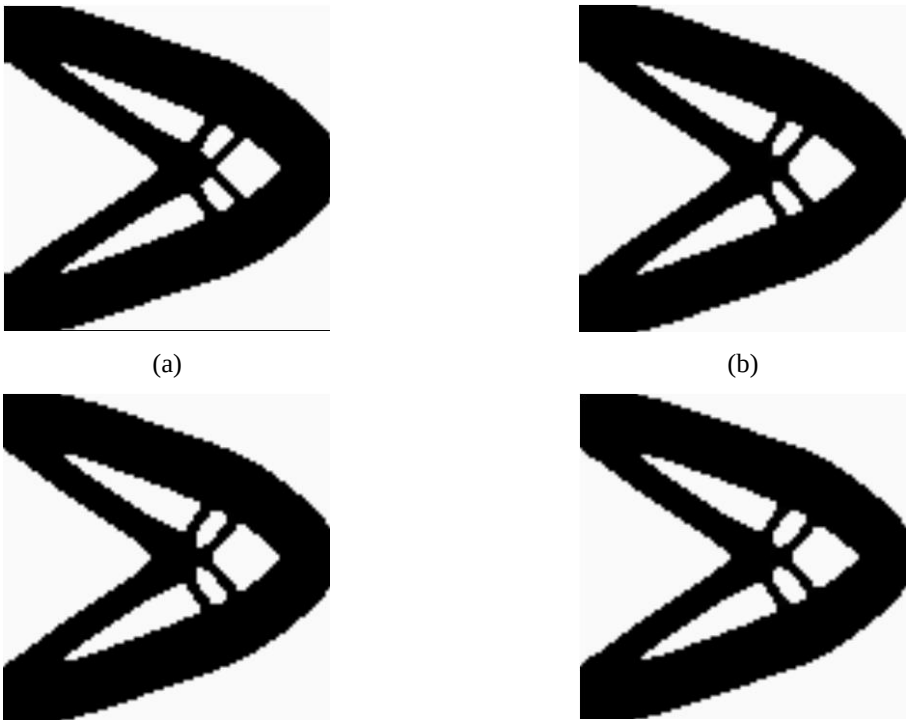

(a) (b)

(c) (d)

Figure 13: Optimal topology for $100 \times 100$ material points with various horizon sizes, the conical bond function and with the projection operator. (a) Horizon 2Δ (iteration 1653). (b) Horizon 3Δ (iteration 1653). (c) Horizon 4Δ (iteration 1803). (d) Horizon 5Δ (iteration 1803).

Table 1: Comparison of different horizon sizes when implementing the conical bond function and the projection operator (* the computational cost is normalized with the computational cost of the 2Δ** model obtained without the projection operator).

| Horizon size | Iterations required for the optimal topology | Computational cost factor* | Optimal strain energy density |
|---|---|---|---|
| 2Δ** | 45 | 1 | 0.1291865393E+03 |
| 2Δ | 1653 | 15.4 | 0.1252024314E+03 |
| 3Δ | 1653 | 62.8 | 0.1170160366E+03 |
| 4Δ | 1803 | 146.3 | 0.1174412304E+03 |
| 5Δ | 1803 | 168.4 | 0.1206488985E+03 |

From Figure 13, all the optimal topological results are almost similar regardless to the selection of the horizon size. Looking into Table 1, the optimal value of the total strain energy density is obtained when using a horizon size 3Δ. However, the computational cost required by the 3Δ model is almost four times larger than what is required by the 2Δ model. As the non-gradient heuristic topology optimization method is already less efficient in terms of speed when compared against the gradient-based topology optimization methods, it is more practical to use a horizon size of 2Δ especially since both models provide almost the same result. In addition, a phenomenon that develops when using a horizon size greater than 2Δ is presented in the next section.

## 4.2 Case 2: 2:1 cantilever beam subjected to a point load at the middle of the free end

A similar cantilever beam is subjected to a point load at the middle of the free end is shown in Figure 14. The beam has a length to width ratio of 2:1. The exact same parameters and techniques are employed as in the last section.

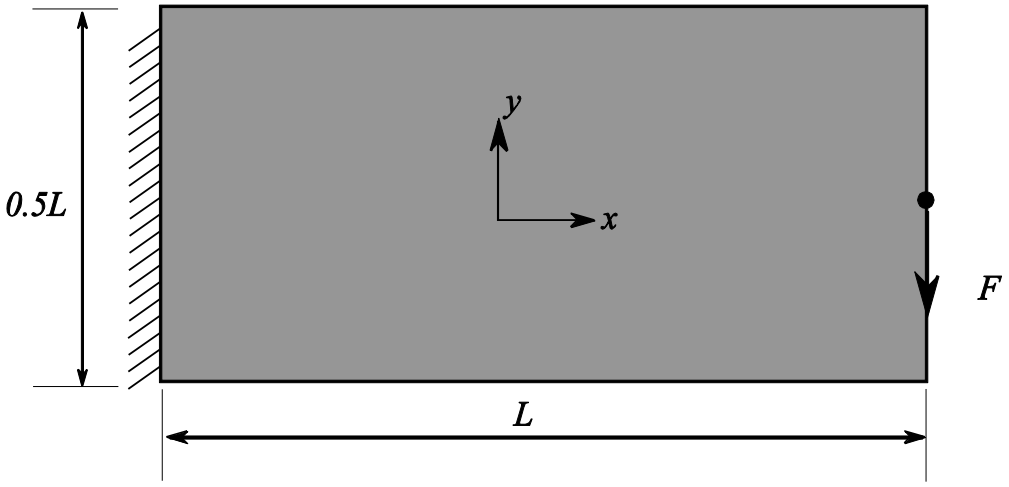


Figure 14: Geometry and loading for the 2:1 length to width ratio cantilever beam with a load at the middle of the free end.

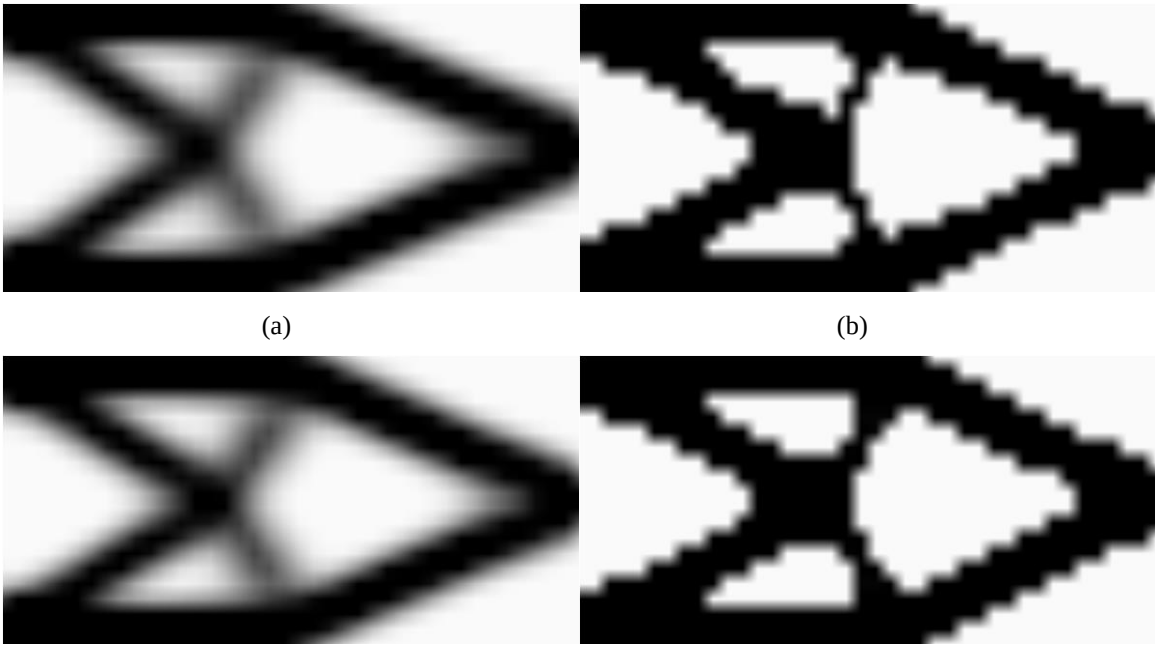


Figure 15: Optimal topologies for $40 \times 20$ material points with a horizon size $2\Delta$. (a)Without the conical bond function and the projection operator (iteration 198). (b) Without the conical bond function and with the projection operator (iteration 252). (c) With the conical bond function and with the projection operator (iteration 171). (d) With the conical bond function and with the projection operator (iteration 252).

The topological results for the $40 \times 20$ cantilever beam subjected to a point load at the middle of the free end are shown in Figure 15. The PD optimal topological result for the $40 \times 20$ cantilever beam when the conical bond function and the projection operator are

employed is compared with the results obtained by Smoothed Particle Hydrodynamics (SPH) and Meshless Galerkin in Figure 16. One may clearly find that the current PD approach has a better presentation of the solid and the void material regions.

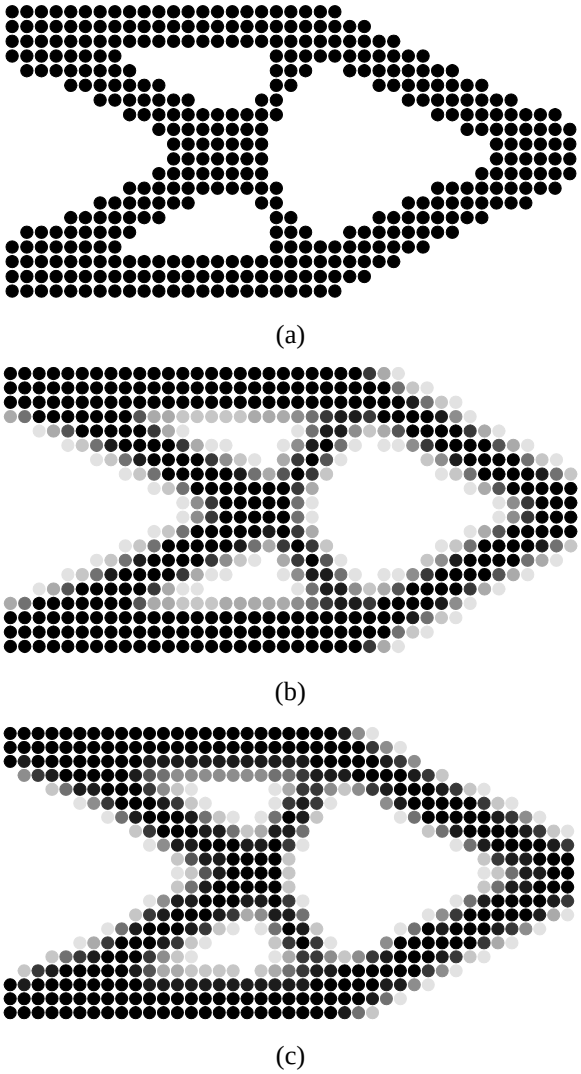

(a)

(b)

(c)

Figure 16: Comparison of the optimal topological results generated by various meshless methods. (a) PD 40×20. (b) SPH 40×20 regenerated from [101]. (c) Meshless Galerkin 41×21 regenerated from [101].

Two additional models are discretized into uniformly distributed volumetric material points of $80 \times 40$ and $100 \times 50$ are presented. For this specific geometry and loading condition the topological results obtained for the $40 \times 20$, $80 \times 40$ and $100 \times 50$ models shown in Figure 15, Figure 17 and Figure 18, respectively, are nearly similar. However, there is a linear improvement in the quality of the topological details with the increase on the number of material points. Note that a model's optimal strain energy (not strain energy

density) value decreases and its stiffness increases with the increase on the number of material points used. In Figure 19, for various models, a graph is showing the decrease in the strain energy densities in accordance to the optimization iterations.

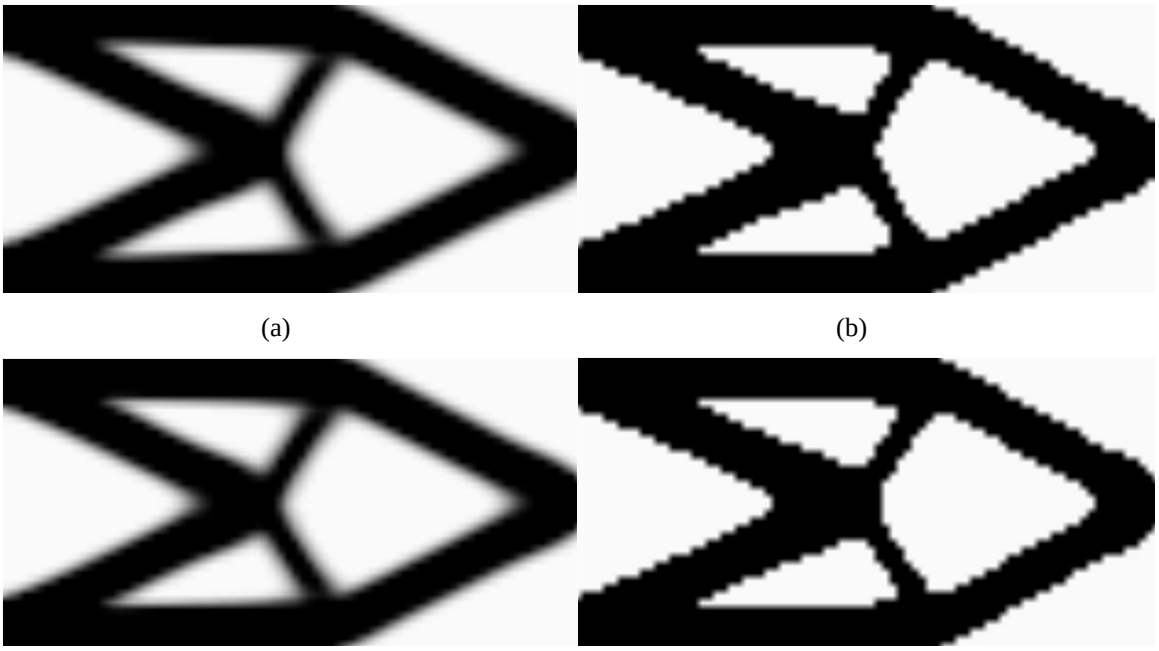

(a) (b)

(c) (d)

Figure 17: Optimal topologies for $80 \times 40$ material points with a horizon size $2\Delta$. (a) Without the conical bond function and the projection operator (iteration 411). (b) Without the conical bond function and with the projection operator (iteration 252). (c) With the conical bond function and without the projection operator (iteration 618). (d) With the conical bond function and with the projection operator (iteration 252).

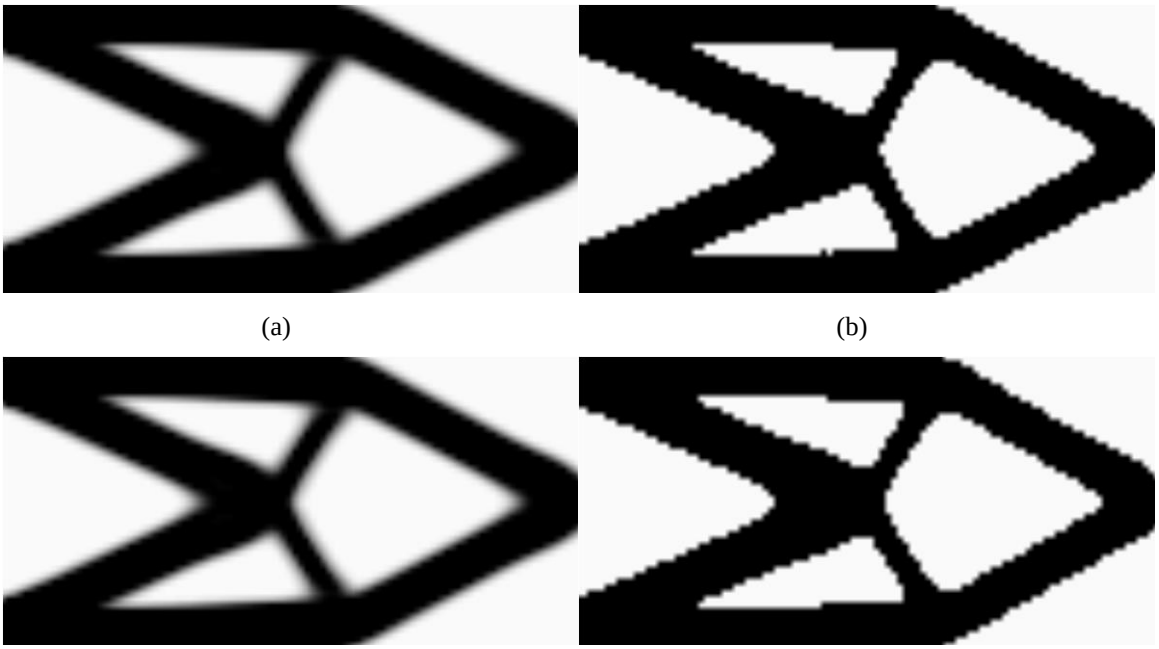

(a) (b)

(c) (d)

Figure 18: Optimal topologies for $100 \times 50$ material points with a horizon size $2\Delta$. (a) Without the conical bond function and the projection operator (iteration 579). (b) Without the conical bond function and with the projection operator (iteration 252). (c) With the conical bond function and without the projection operator (iteration 387). (d) With the conical bond function and with the projection operator (iteration 252).

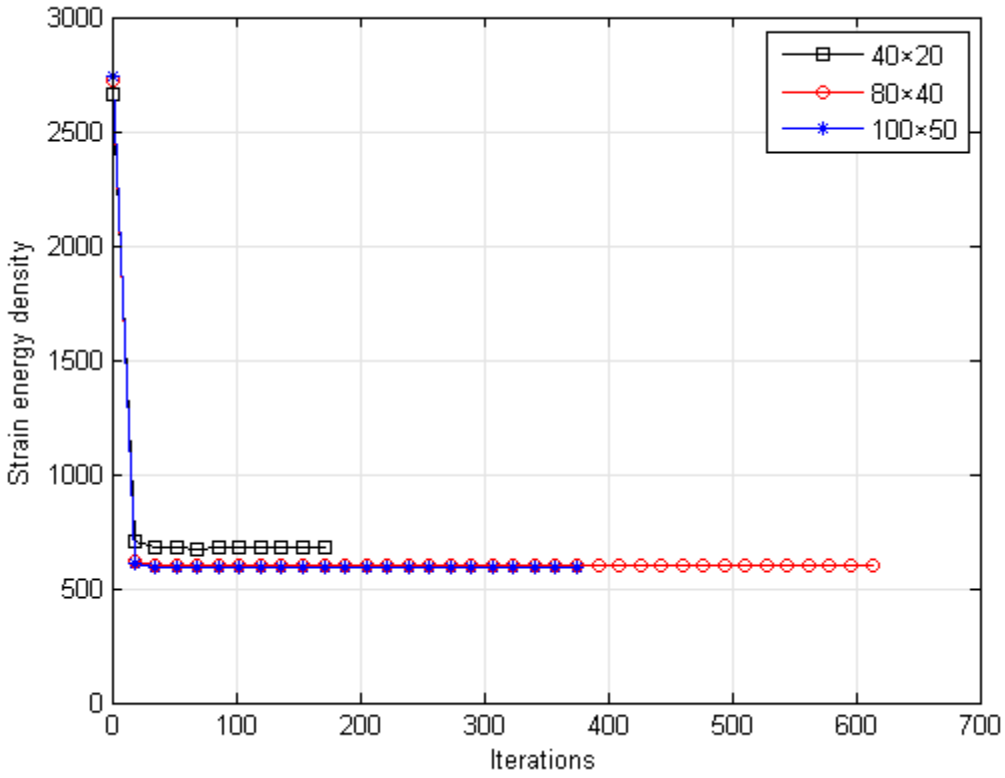


Figure 19: Strain energy density convergence for different number of material points

The optimal topological results obtained using various volume constraints for the $100 \times 50$ model are proposed in Figure 20. The conical bond function is employed while considering a 0.15 increment increase of the projection parameters $\beta$ every 50 iteration. The results obtained from the current PD approach are compared with optimal topological results developed using an FEM based topology optimization tool published in [86]. The FEM model is discretized into $100 \times 50$ elements with a penalization coefficient of 3. The PD topological results show a good agreement with the FEM optimal topologies. However, the discreteness of the all optimal topologies obtained by FEM is always higher than 15 %.

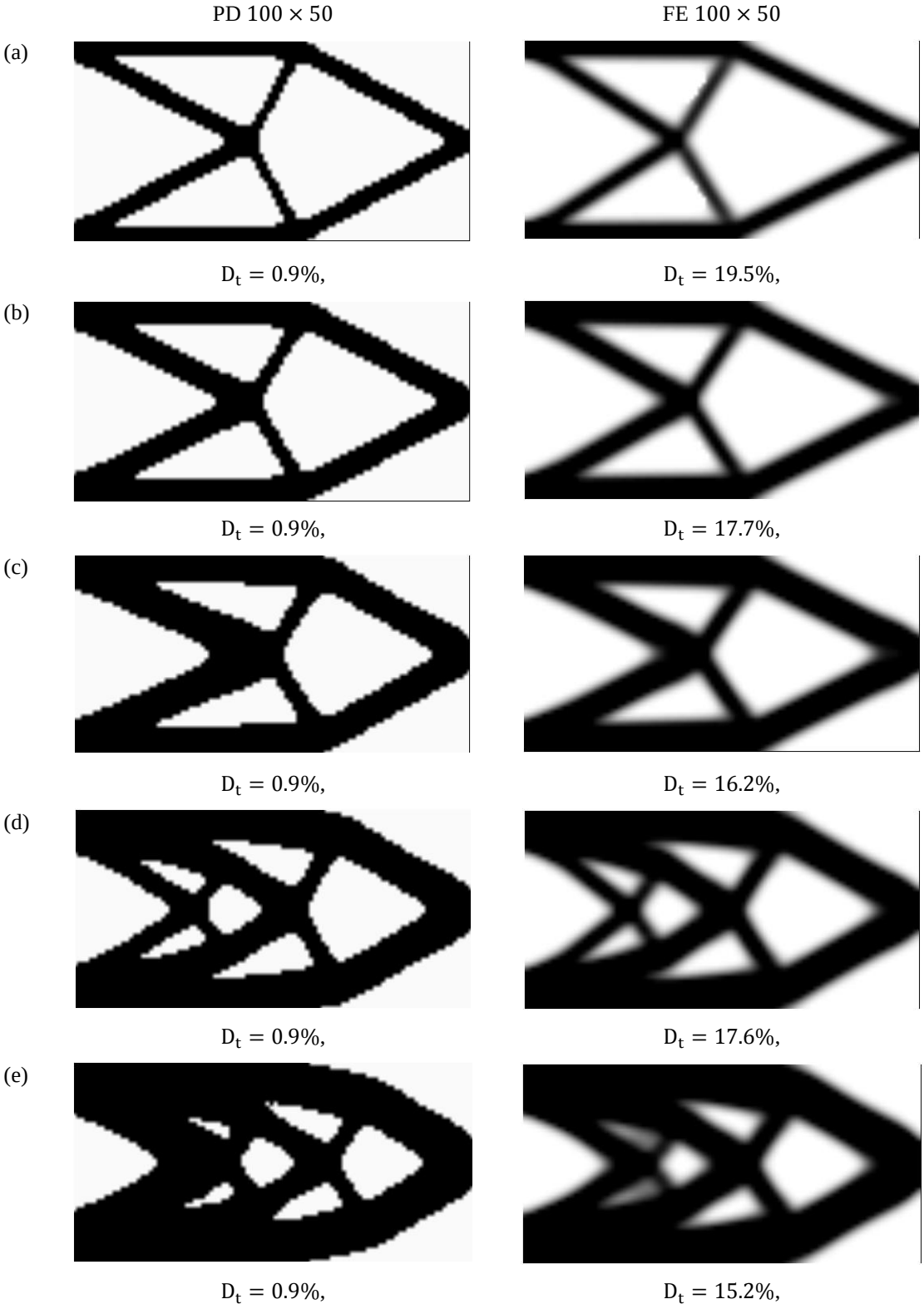


Figure 20: Optimal topologies using different volume constraints on $100 \times 50$. (a) 30%, (b) 40%, (c) 50%, (d) 60% and (e) 70 % volume constraints.

In the following, a supplementary discussion on an additional benefit behind employing a horizon size of $2\Delta$ regardless to the reduction in the computational cost is presented. Frequently, when using a horizon size larger than $2\Delta$, a phenomenon similar to the original checkerboard phenomenon shown in Figure 21 occurs; it is usually solved when employing the PD conical bond function. However, the main reason behind such a phenomena is unknown and undiscussed in the literature. One of the expected reasons is the possibility of having a conflict between the PD horizon size and the density filter radius.

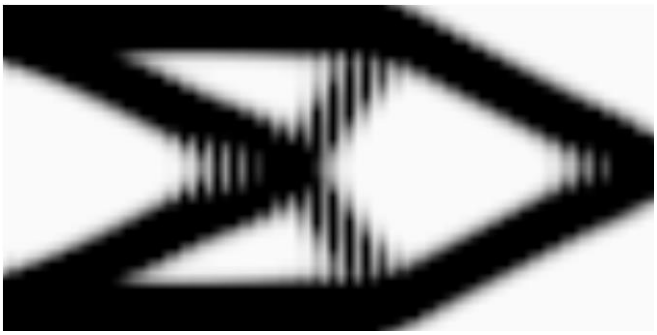

Figure 21: Optimal topology for $80 \times 40$ material points with a horizon size of $3\Delta$ without employing the conical bond function and the projection operator

## 4.3 Case 3: 1:1 cantilever beam subjected to a point load at the bottom corner of the free end

In this case, a cantilever beam is subjected to a point load at the bottom corner of the free end is shown in Figure 22. The beam has a length to width ratio of 1:1. The exact same parameters and techniques are employed as in case 1. Four models are discretized into uniformly distributed volumetric material points of $22 \times 22, 44 \times 44, 66 \times 66$ and $100 \times 100$.

In Figure 23, the optimal topological results for the $22 \times 22$ material points beam at various volume constraints when applying the conical bond function are shown. All the $22 \times 22$ examples consider a 0.25 increment increase of the projection parameters $\beta$ every 50 iteration if the projection operator is applied.

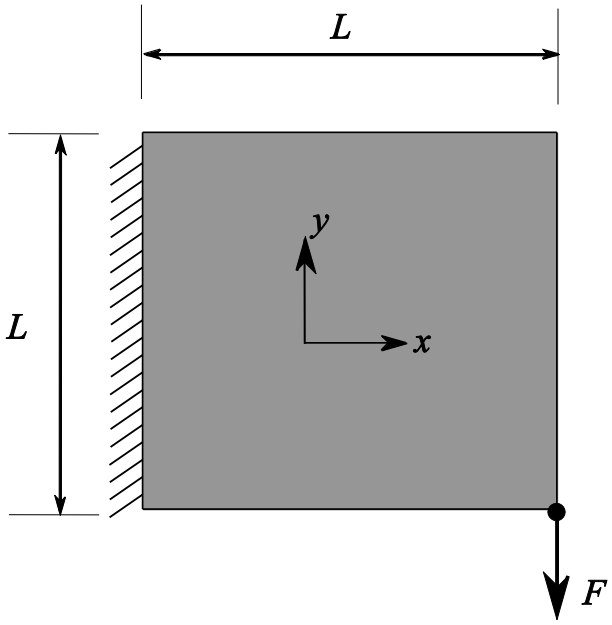


Figure 22: Geometry and loading for the 1:1 length to width ratio cantilever beam with a load at the bottom corner of the free end

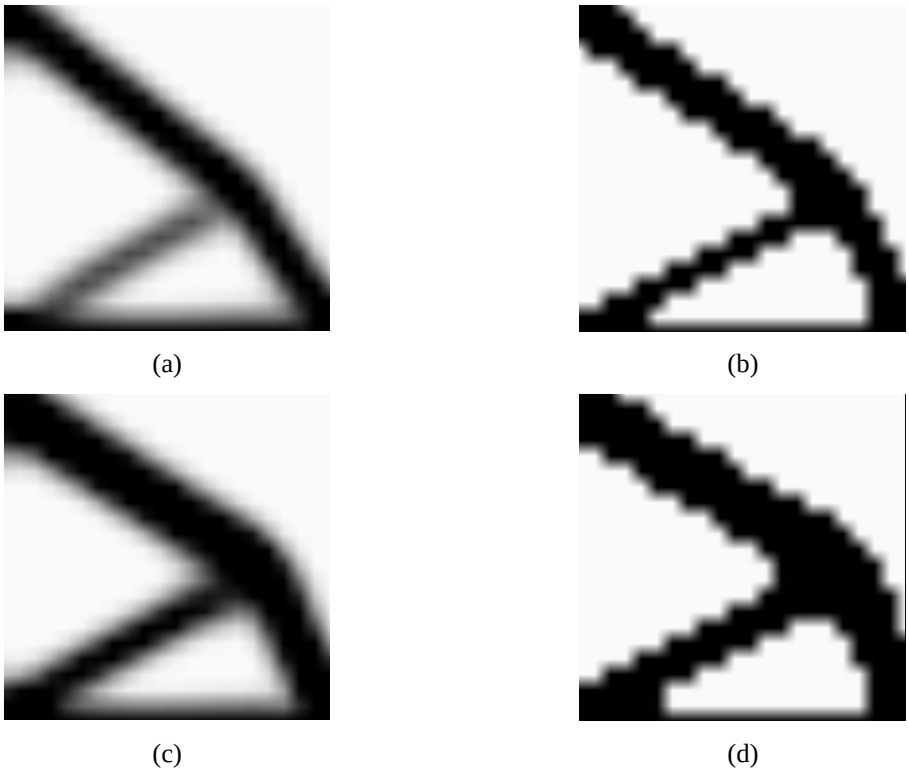

(a) (b)

(c) (d)

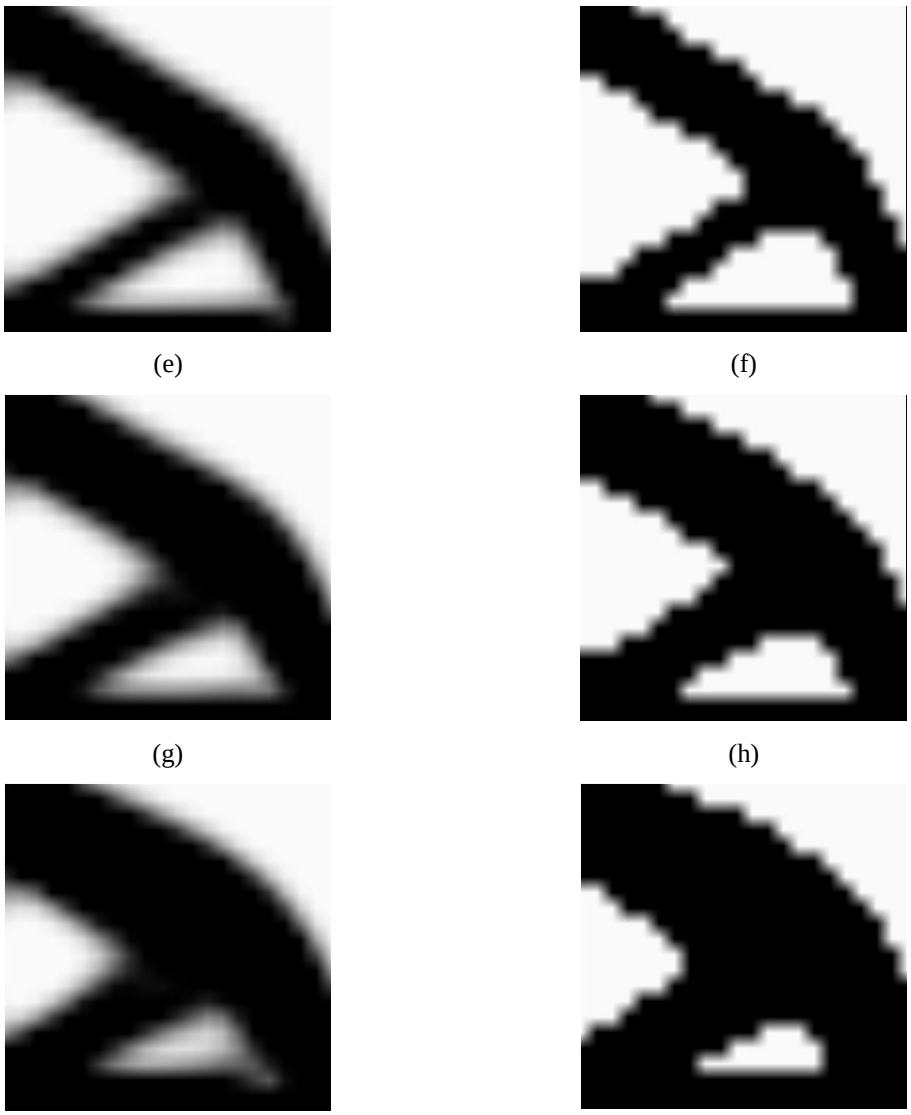

(e) (f)

(g) (h)

(i) (j)

Figure 23: Optimal topologies with various volume constraints for 22×22 material points with a horizon size 2Δ when load is at bottom corner. (a) 30% volume constraint (iteration 150). (b) 30% volume constraint (iteration 453) with the projection operator. (c) 40% volume constraint (iteration 78). (d) 40% volume constraint (iteration 453) with the projection operator. (e) 50% volume constraint (iteration 90). (f) 50% volume constraint (iteration 453) with the projection operator. (g) 60% volume constraint (iteration 39). (h) 60% volume constraint (iteration 402) with the projection operator. (i) 70% volume constraint (iteration 51). (j) 70% volume constraint (iteration 402) with the projection operator.

As discussed earlier, the employment of the conical bond function does not affect the optimization process negatively and it converges the PD results. Depending on the geometry and the loading condition, the use of the conical bond function may also play an important role in providing a larger design space without the need of increasing the number of material points used in a problem. The optimal topological results for the $44 \times 44$ model

with and without the use of the conical bond function are shown in Figure 24 and one may notice the difference. The results are developed using the same optimization stopping criteria.

(a) (b)

Figure 24: Optimal topologies for $44 \times 44$ material points with a horizon size $2\Delta$ when load is at the bottom corner. (a) Without the conical bond function and the projection operator (iteration 168). (b) With the conical bond function and without the projection operator (iteration 1413).

The optimal topological results for a $66 \times 66$ material points beam are shown in Figure 25 using various projection conditions. Recalling, sometimes the increase on the number of material points may not alter the final topological result. However, there is a linear improvement in the topological details. Comparing the results shown in Figure 24.b and Figure 25.d, one may clearly find significant topological similarity. Note that, the number of iterations required by the $66 \times 66$ model to obtain the optimal topological result is almost 40% less than the number of iterations required by the $44 \times 44$ model. In topology optimization, such a coincident is normal and is resulted from the weak and slow ability of some smaller models to generate an advanced topology.

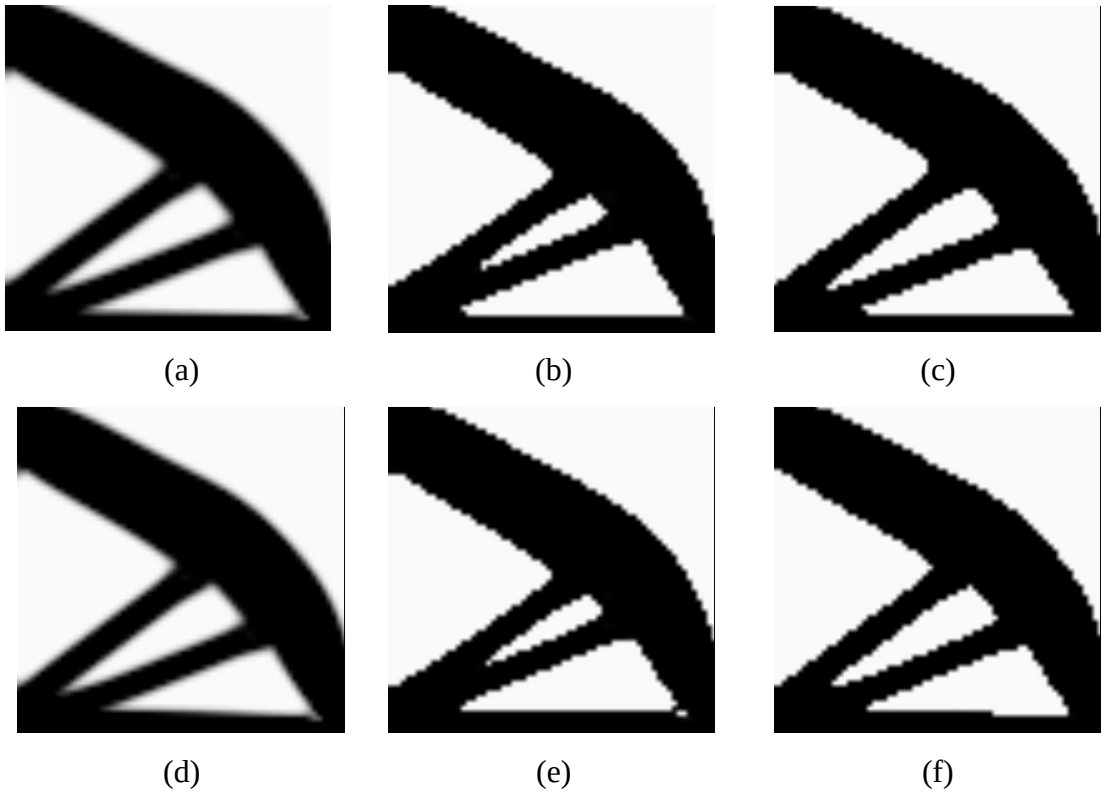


Figure 25: Optimal topologies for $66 \times 66$ material points with a horizon size $2\Delta$ when load is at the bottom corner. (a) Without the conical bond function and the projection operator (iteration 516). (b) Without the conical bond function and with the projection operator (iteration 354) with a projection parameter $\beta$ increase of 0.25 every 50 iterations. (c) Without the conical bond function and with the projection operator (iteration 1803) with a projection parameter $\beta$ increase of 0.15 every 150 iterations. (d) With the conical bond function and without the projection operator (iteration 867). (e) With the conical bond function and with the projection operator (iteration 354) with a projection parameter $\beta$ increase of 0.25 every 50 iterations. (f) With the conical bond function and with projection operator (iteration 1803) with a projection parameter $\beta$ increase of 0.15 every 150 iterations.

The fact that the projection operator could influence the final topological result by adding unneeded material regions is discussed earlier. Accordingly, it is advised that the increment increase of the projection parameter $\beta$ should be small and the number of iterations between the sequence increases of the projection parameter $\beta$ should be large. For the $66 \times 66$ model, projection conditions of a 0.25 increase of the projection parameter $\beta$ every 50 iterations and a 0.15 increase every 150 iterations are employed to obtain the results shown in Figure 25.b and Figure 25.e ,and shown in Figure 25.c and Figure 25.f, respectively. After comparing the developed topologies with the ones obtained without the projection operator shown in Figure 25.a and Figure 25.d, one may clearly find that using a smaller increment increase of the projection parameter $\beta$ with a larger number of iterations between the sequence increases prevents stopping the development process of the topology early.

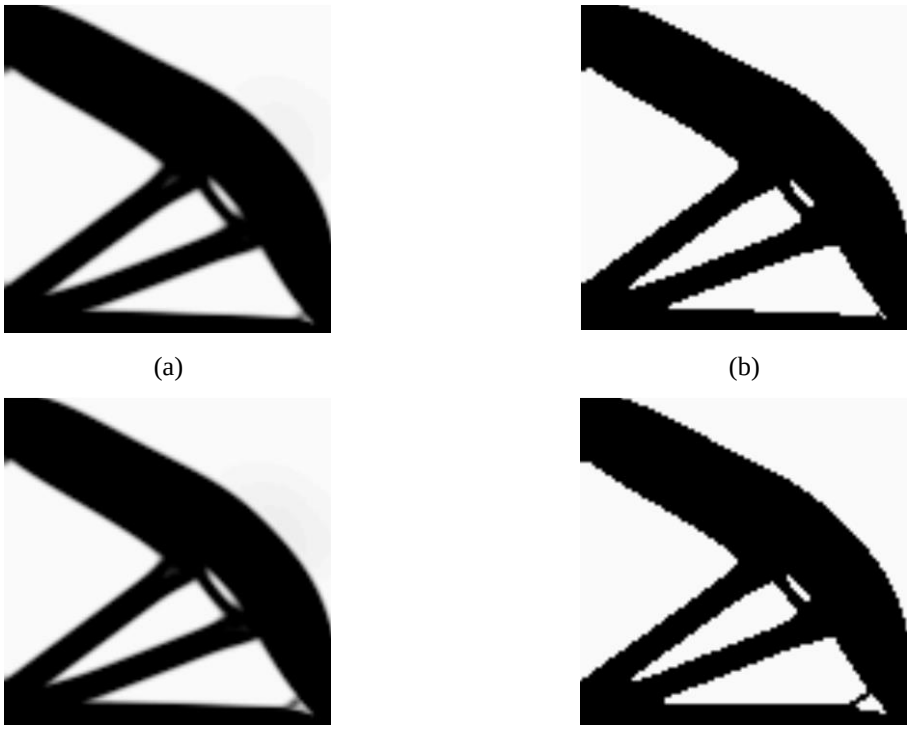

(a) (b)

(c) (d)

Figure 26: Optimal topologies for $100 \times 100$ material points with a horizon size $2\Delta$ when load is at the bottom corner. (a) Without the conical bond function and the projection operator (iteration 1317). (b) Without the conical bond function and with the projection operator (iteration 1653). (c) With the conical bond function and without the projection operator (iteration 1107). (d) With the conical bond function and with the projection operator (iteration 1653).

The optimal topological results for the $100 \times 100$ material points beam are shown in Figure 26. All the $100 \times 100$ examples consider a 0.15 increment increase of the projection parameters $\beta$ every 150 iteration if the projection operator is applied. In Figure 27, various topological results are shown for models discretized into different number of material points. As mentioned before, a stiffer topology should develop with the increase of the number of material points while considering the fact that some topologies could be hard to manufacture. To illustrate the relation between the stiffness of the topology and the number of material points, Table 2 provides a comparison between the models in terms of the tip deflection. Consequently, one may clearly find that the tip deflection decreases with the increase of the number of material points. The topology obtained for the $100 \times 100$ material point model is only subjected to 30% of the tip deflection that the $25 \times 25$ material point model undergo. Correspondingly, the increase in the number of material points linearly increase the computational cost required by the model.

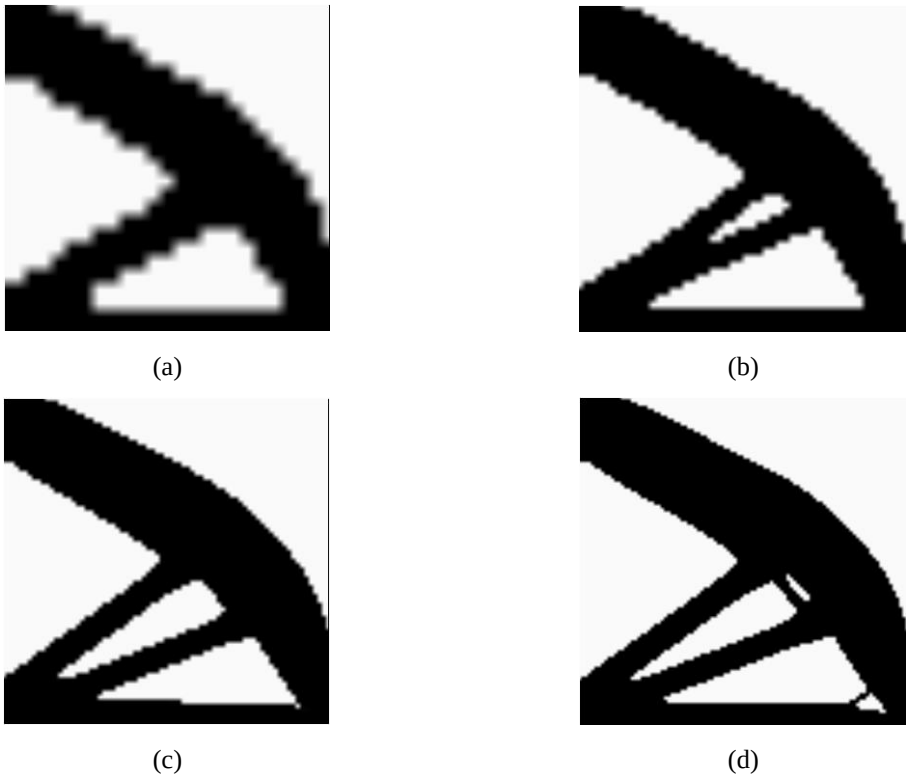

(a) (b)

(c) (d)

Figure 27: Optimal topologies for various numbers of material points with a horizon size 2Δ when load is at the bottom corner. (a) $25 \times 25$. (b) $50 \times 50$. (c) $75 \times 75$. (d) $100 \times 100$.

Table 2: Comparison of different material points number when implementing the conical bond function and the projection operator (* the computational cost and the tip deflection is normalized with the computational cost and the tip deflection of the 25×25.

| Material points number | Computational cost factor* | Tip deflection factor* |
|---|---|---|
| $25 \times 25$ | 1 | 1 |
| $50 \times 50$ | 10.4 | 0.89 |
| $75 \times 75$ | 25.1 | 0.37 |
| $100 \times 100$ | 68.6 | 0.30 |

### 4.4 Case 4: 2:1 cantilever beam subjected to a point load at the bottom corner of the free end

Another cantilever beam is subjected to a point load at the bottom corner of the free end is shown in Figure 28. The exact same parameters and techniques are employed as in case 1. Four models are discretized into uniformly distributed volumetric material points of $40 \times 20$, $100 \times 50$, $140 \times 70$ and $160 \times 80$. The optimal topological results for the $40 \times$

20 material points beam are shown in Figure 29. A 0.15 increment increase of the projection parameters $\beta$ every 120 iterations is applied.

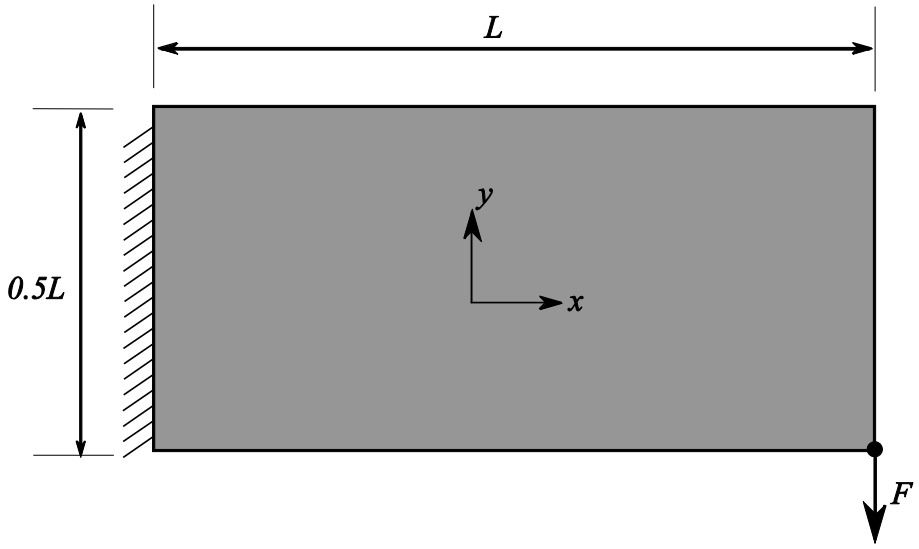


Figure 28: Geometry and loading for the 2:1 length to width ratio cantilever beam with a load at the bottom corner of the free end.

For this particular geometry and loading condition, most of the obtained optimal topological results experience another phenomena similar to the original checkerboard phenomena. The well-known checkerboard phenomena mainly result from either neglecting the use of a filter or reducing the filter's radius close to zero. Therefore, the topology is affected and obliged to develop a checkerboard pattern to represent most of the solid material regions. In this study, a checkerboard pattern appear along the rectangular boundary, however, the overall efficiency of the optimal topology is not affected. Note that, when reducing the filter radius close to zero, the boundary pattern disappear, while, the original checkerboard phenomena develop as shown in Figure 30.

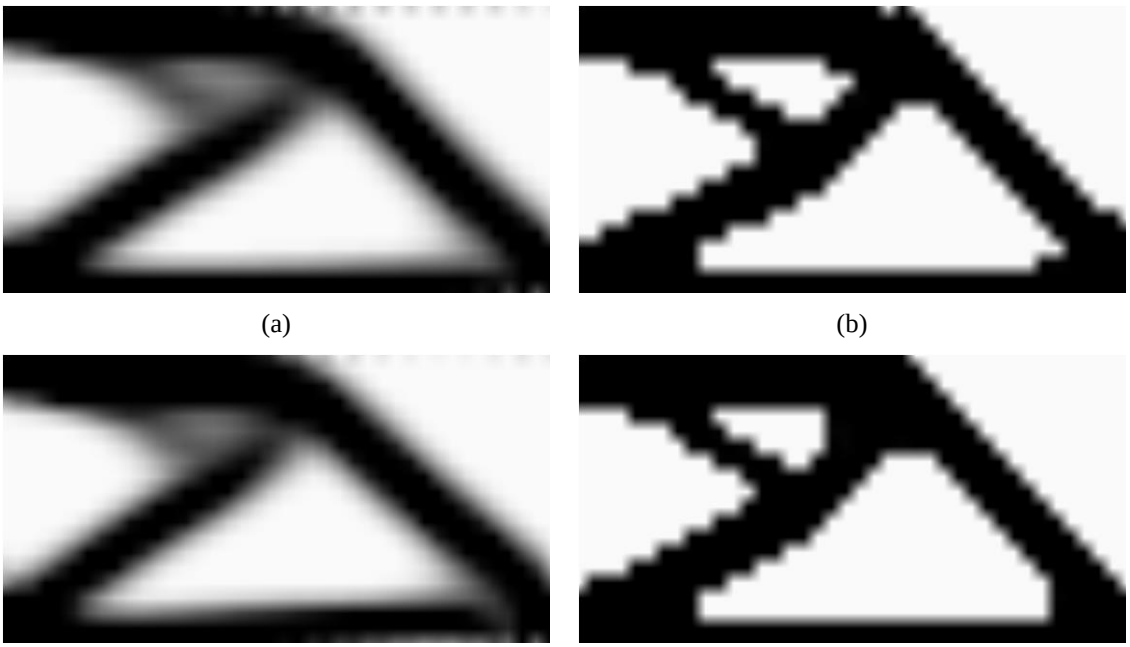

(a) (b)

(c) (d)

Figure 29: Optimal topologies for $40 \times 20$ material points with a horizon size $2\Delta$ when load is at the bottom corner. (a) Without the conical bond function and the projection operator (iteration 177). (b) Without the conical bond function and with the projection operator (iteration 1683). (c) With the conical bond function and without the projection operator (iteration 204). (d) With the conical bond function and with the projection operator (iteration 1683).

Figure 30: Optimal topology for $40 \times 20$ material points with a horizon size $2\Delta$ and a filter radius 0.5.

In the literature, a phenomenon similar to the presented in this thesis is not discussed. These patterns appearing along the boundary vanish as a whole or a part when employing the projection operator as shown in the results from Figure 29.d and Figure 31.d, respectively, however, one should not consider this technique as a solution. For the $100 \times 50$ material point model, the optimal topological results are shown in Figure 31. A 0.15 increment increase of the projection parameters $\beta$ every 150 iterations is considered. In addition, the optimal topological results for the $100 \times 50$ material point model using

various volume constraints are shown in Figure 32 and a 0.15 increment increase of the projection parameters $\beta$ every 200 iterations is considered.

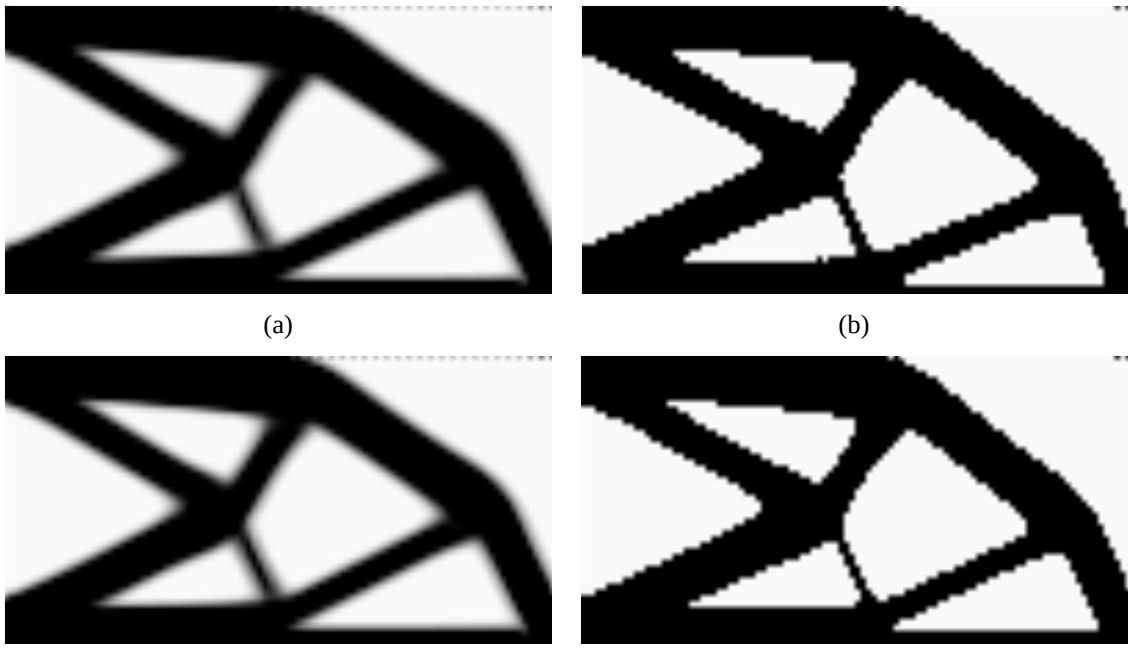

(a) (b)

(c) (d)

Figure 31: Optimal topologies for $100 \times 50$ material points with a horizon size $2\Delta$ when load is at the bottom corner. (a) Without the conical bond function and the projection operator (iteration 1683). (b) Without the conical bond function and with the projection operator (iteration 1953). (c) With the conical bond function and without the projection operator (iteration 1053). (d) With the conical bond function and with the projection operator (iteration 1803).

(a) (b)

Figure 32: Optimal topologies with various volume constraints for $100 \times 50$ material points with a horizon size $2\Delta$, the conical bond function and the projection operator when load is at bottom corner. (a) 30% volume constraint (iteration 2403). (b) 70% volume constraint (iteration 2403).

As discussed before, using the conical bond function over the constant bond function sometimes help in providing a larger design space. To demonstrate, Figure 33 shows the

optimal topological result obtained for a $140 \times 70$ model employing a conical bond function. On the other hand, Figure 34.a shows the optimal topological result for a $160 \times 80$ model employing a constant bond function. Although, the $160 \times 80$ model utilizes 3000 additional material points than the $140 \times 70$ model, one may clearly find that the optimal topological results are similar. Furthermore, Figure 34.b shows the optimal topological result for a $160 \times 80$ model employing a conical bond function. Comparing results from Figure 34, one may notice the significant difference between both the optimal topological results. An advanced topology is developed and obtained when employing the conical bond function.

Figure 33: Optimal topology for $140 \times 70$ material points with a horizon size $2\Delta$ when load is at the bottom corner with the conical bond function and without the projection operator (iteration 1638).

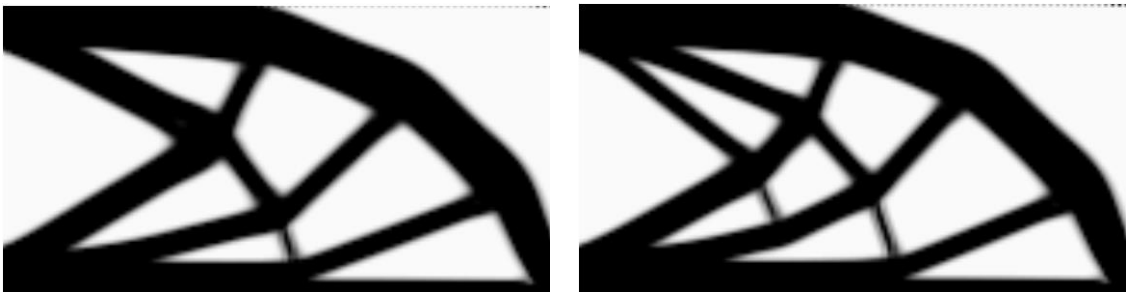

(a) (b)

Figure 34: Optimal topology for $160 \times 80$ material points with a horizon size $2\Delta$ when load is at the bottom corner. (a) Without the conical bond function and the projection operator (iteration 2079). (b) With the conical bond function and without the projection operator (iteration 1407).

## 4.5 Case 5: L bracket

As the topology optimization of L bracket is frequently used in the literature, the geometry and loading condition for L bracket subjected to a point load is shown in Figure 35. The L-bracket has a dimension of length for the long edge and 0.4 the length for the short edge. The exact same parameters and techniques are employed as in case 1, however, a 0.15 increment increase of the projection parameters $\beta$ every 100 iterations is considered.

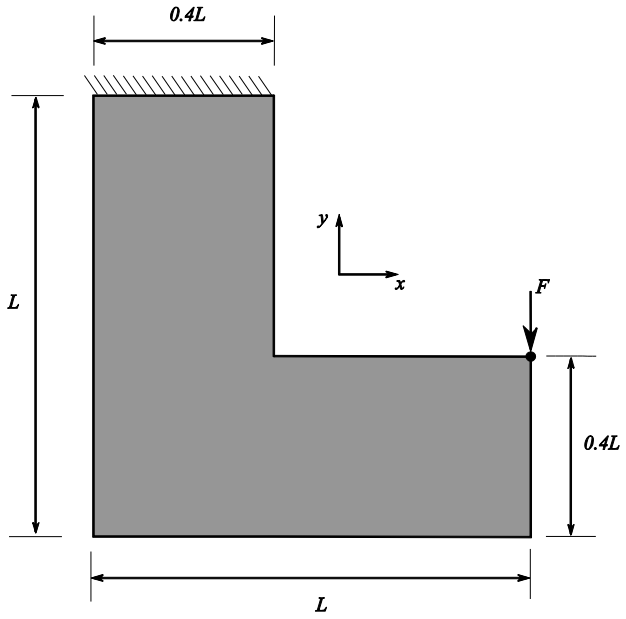


Figure 35: Geometry and loading of L bracket.

Several models are discretized into uniformly distributed volumetric material points of $50 \times 20, 60 \times 24, 80 \times 32$ and $100 \times 40$. The obtained topological results for all models are shown in Figure 36. As expected and proven earlier, the developed topology utilizes the increase on the number of material points to become stiffer. Visually, this improvement is illustrated in the development of extra supporting links for the structure.

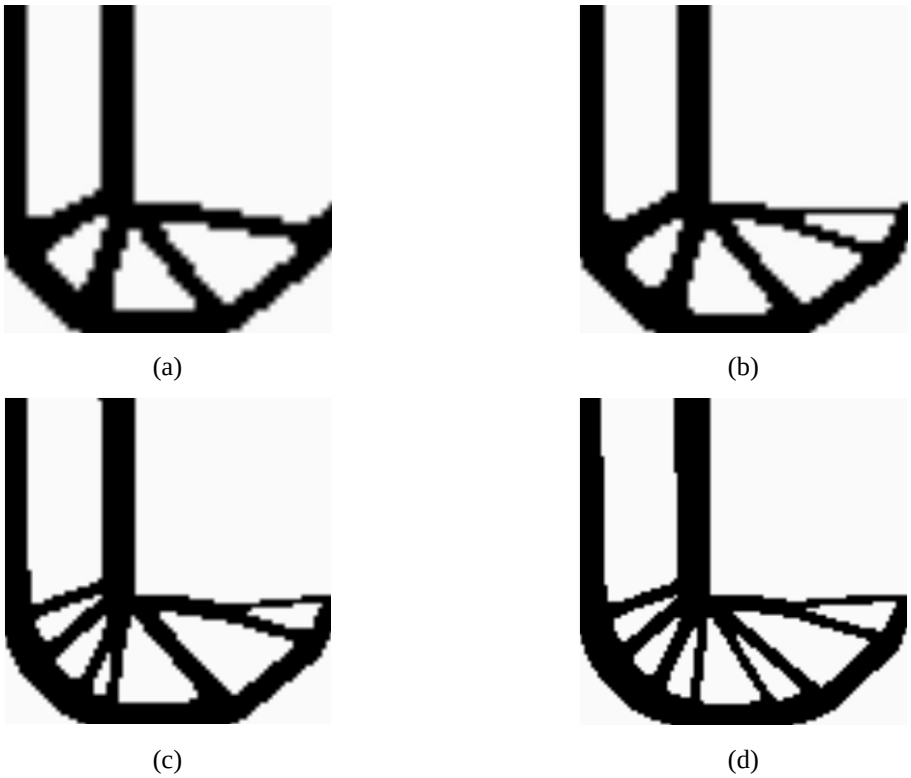

(a) (b)

(c) (d)

Figure 36: Optimal topologies of L bracket for various numbers of material points with a horizon size $2\Delta$. (a) $50 \times 20$ (iteration 1203) with the conical bond function and the projection operator. (b) $60 \times 24$ (iteration 1203) with the conical bond function and the projection operator (c) $80 \times 32$ (iteration 1203) with the conical bond function and the projection operator (d) $100 \times 40$ (iteration 1104) with the conical bond function and the projection operator.

Moreover, to look into the development process of an optimal topology and the progress of the projection operator, an iteration analysis of the optimal topology for the $100 \times 40$ L bracket is shown in Figure 37. From iteration 3 to iteration 9, the main structure of the topology starts to develop after specifying both the material and the void regions. The discreteness starts at 39.5% and decreases rapidly to 11.7% with the iteration increase. Starting from iteration 15 to iteration 450, some solid material regions split into multiple regions with an expansion of the void material regions in between. This slow process aims for reaching a topological stability and the discreteness changes from 6.4% to 5.2%. The developed topology is then influenced by the projection operator until reaching iteration 1104 with a discreteness of 0.9%. Note that, the results obtained on iteration 450 and iteration 1104 are almost similar, however, gray material regions are vanished completely.

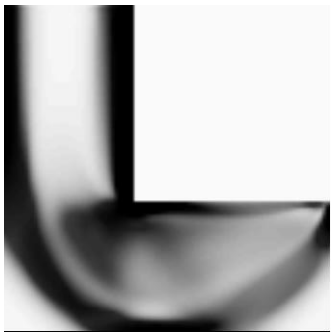

Iteration 3, $D_t = 39.5\%$,

Iteration 30, $D_t = 6.4\%$,

Iteration 6, $D_t = 22.2\%$,

Iteration 150, $D_t = 6.4\%$,

Iteration 9, $D_t = 11.7\%$,

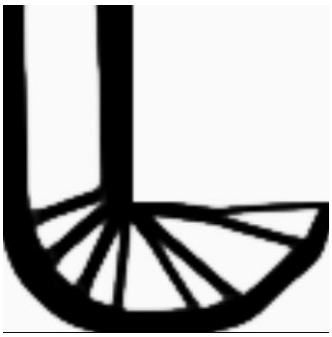

Iteration 450, $D_t = 5.2\%$,

Iteration 15, $D_t = 6.6\%$,

Iteration 1104, $D_t = 0.9\%$,

Figure 37: Iteration analysis of optimal topology for $100 \times 40$ L bracket.

## 4.6 Case 6: 2:1 cantilever beam with a hole subjected to a point load at the middle of the free end

The geometry and loading condition for a 2:1 length to width ratio cantilever beam with a hole subjected to a point load at the middle of the free end is shown in Figure 38. The purpose of studying this case is to test the potential of the proposed method in different geometrical conditions. When considering realistic boundary and loading conditions (note that these conditions are neglected here) similar geometries could be optimized and used based on a variety of applications, for example in pipe support. The exact same parameters and techniques are employed as in case 5.

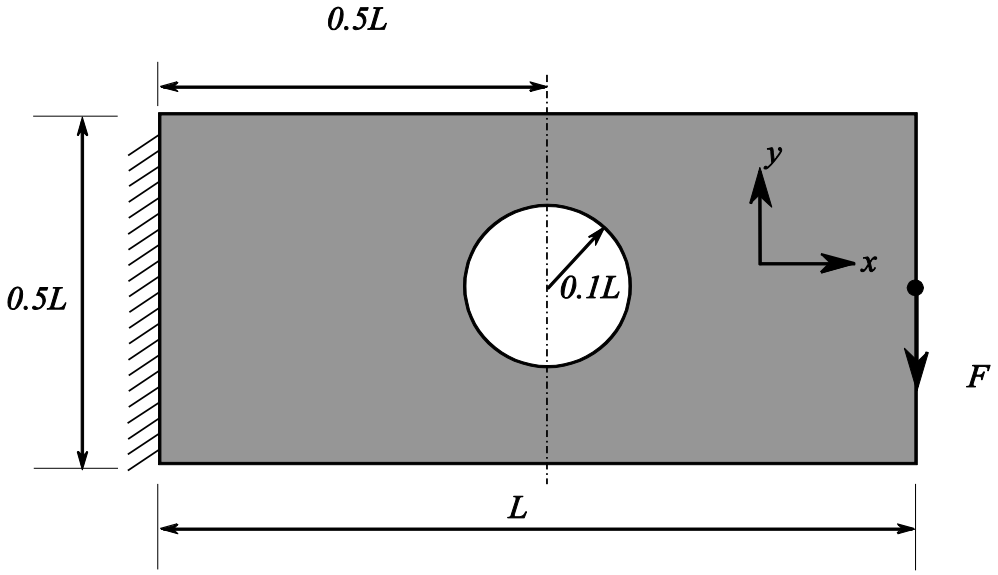


Figure 38: Geometry and loading for the 2:1 length to width ratio cantilever beam with hole and a load at the middle of the free end.

In Figure 39, the optimal topological results for the 2:1 length to width ratio cantilever beam with a hole are shown. Models are discretized into $80 \times 40$ and $100 \times 50$ uniformly distributed material points. To study the effect of the presence of the hole within the structure, the developed topologies are compared with different topologies shown in Figure 40, obtained for an identical case without a hole. Accordingly, one may clearly find the development of additional supporting links around the position of the hole.

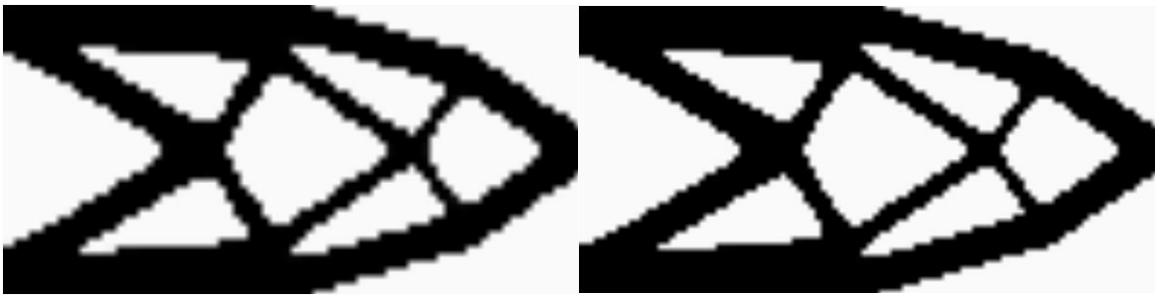

(a) (b)

Figure 39: Optimal topologies for the 2:1 length to width ratio cantilever beam with hole and a load at the middle of the free end using various numbers of material points with a horizon size $2\Delta$. (a) $80 \times 40$ (iteration 1302) with the conical bond function and the projection operator. (b) $100 \times 50$ (iteration 1203) with the conical bond function and the projection operator.

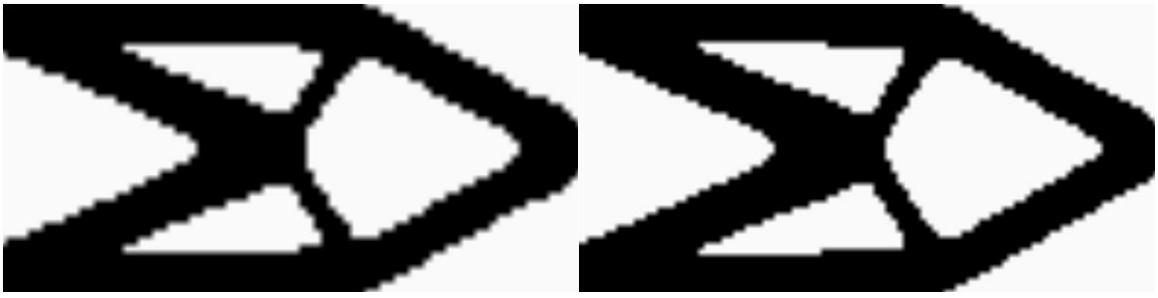

(a) (b)

Figure 40: Optimal topologies for the 2:1 length to width ratio cantilever beam without hole and a load at the middle of the free end using various numbers of material points with a horizon size $2\Delta$. (a) $80 \times 40$. (b) $100 \times 50$.

To represent material points from the $100 \times 50$ material point model in terms of the strain energy density, Figure 41 shows an image of scaled colors displaying each material point according to its relative strain energy density value. As expected, the highest strain energy density within the structure is around the loading position and the corners of the fixed edge.

Figure 41: Strain energy density representation using scaled colors.

## 4.7 Case 7: 1:1 Plate hinged from all corners and subjected to a point load at the middle of the top edge

As a last case, the geometry and loading condition for a 1:1 length to width ratio plate, hinged from all corners and subjected to a point load at the middle of the top edge is shown in Figure 42. The exact same parameters and techniques are employed as in case 1 and a 0.15 increment increase of the projection parameters $\beta$ every 50 iterations is considered. A single model is discretized into $100 \times 100$ uniformly distributed material points. The obtained optimal topological result for the model is shown in Figure 43.

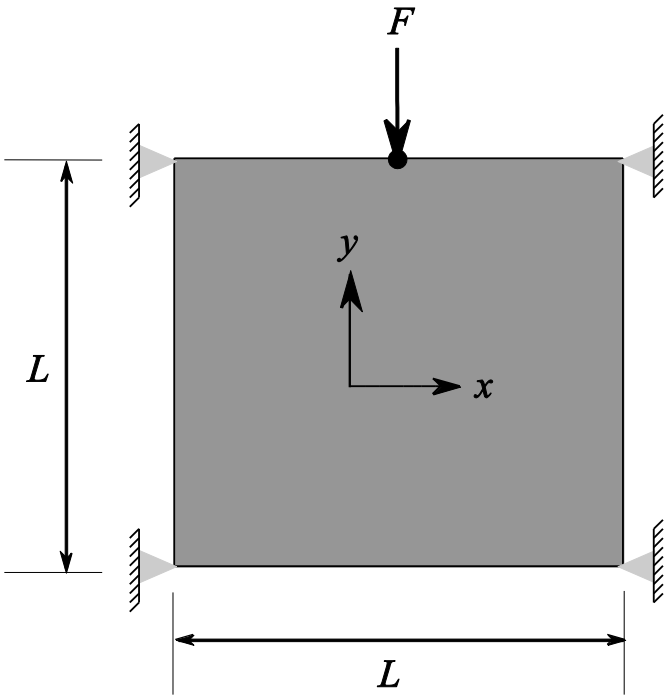


Figure 42: Geometry and loading for the 1:1 length to width ratio plate hinged from all corners.

Figure 43: Optimal topology for a $100 \times 100$ plate hinged from all corners with a horizon size $2\Delta$ (iteration 501).

# 5 CONCLUSION AND FUTURE WORK

PD is rapidly growing, simple, meshless and nonlocal method that was first introduced to enable modelling of discontinuities in solid mechanics. Beside the accuracy of PD and the complexities associated with the implementation of a discontinuity in a mesh-based model, it is known that meshless methods avoid the conditional mesh deformations appearing in mesh-based models.

In the present work, the potential of PD-based topology optimization approach is explored. While gradient-based optimization methods may provide higher efficiency in terms of the number of iterations required to obtain an optimal result compared to the non-gradient topology optimization methods, non-gradient topology optimization methods are simpler to implement. To achieve an efficient topology optimization process, a method that utilizes a continuous design variable over a discrete design variable has been adopted. The PTO method is a heuristic approach that is efficient, simple and flexible in terms of the objective function. Similar methods are the ESO and the BESO.

Here, a minimization of the PD strain energy density is considered as the objective function while considering continuous material density design variables and a volume constraint.

The material model is implemented using a PD FGM model, A PD conical bond function was utilized to enhance the accuracy and to increase the design space, and the adaptive dynamic relaxation method is employed to solve for a static problem. In PTO, the material is distributed in the model based on a modified SIMP approach. In addition, a Heaviside-type projection operator has been is implemented into the PTO method to impose the design variables into discrete values while the discreteness is considered as the optimization stopping criteria.

The projection scheme has also been explored. A small incremental increase in the projection parameter $\beta$ every large number of iterations is the best to avoid any negative effects on the optimal result.

A horizon size of $2\Delta$ has been used to maintain the nonlocal character of PD and to reduce the computational cost. Furthermore, it is noticed that when using a horizon size larger than $2\Delta$, a phenomenon similar to the original well-known checkerboard phenomenon develops and completely distorts the result; sometimes solved when using the conical bond function. A conflict between the PD horizon and the density filter radius is expected to be the reason behind this phenomenon. However, almost all the results obtained using a horizon size $2\Delta$ reflect the robustness and suitability of the proposed approach, especially when validated against the EFG, SPH, and FEM models.

For future work, the approach presented will be used to find the optimal topologies for structures with discontinuities and an investigation on the semi-checkerboard phenomenon will be considered. Additionally, to reduce the time needed to reach a steady state using the ADR technique, a direct solution could be implemented. Last but not least, the plate formulation of PD proposed in [110] will be considered as it is more adequate to the bond-based PD to capture bending deformation. Finally, a topology optimization software tool that is able to optimize any geometry and condition is also proposed as future work.

# 6 REFERENCES

[1] S. A. Silling, "Reformulation of elasticity theory for discontinuities and long-range forces," (in English), *Journal of the Mechanics and Physics of Solids,* Article vol. 48, no. 1, pp. 175-209, Jan 2000.

[2] S. A. Silling, M. Epton, O. Weckner, J. Xu, and E. Askari, "Peridynamic states and constitutive modeling," (in English), *Journal of Elasticity,* Article vol. 88, no. 2, pp. 151-184, Aug 2007.

[3] E. Kröner, "Elasticity theory of materials with long range cohesive forces," *International Journal of Solids and Structures,* vol. 3, no. 5, pp. 731-742, 1967.

[4] D. Rogula, *Nonlocal theory of material media*. Springer, 2014.

[5] A. C. Eringen and D. Edelen, "On nonlocal elasticity," *International Journal of Engineering Science,* vol. 10, no. 3, pp. 233-248, 1972.

[6] I. A. Kunin, *Elastic media with microstructure I: one-dimensional models*. Springer Science & Business Media, 2012.

[7] E. Madenci and E. Oterkus, *Peridynamic theory and its applications*. Springer, 2014.

[8] T. L. Warren, S. A. Silling, A. Askari, O. Weckner, M. A. Epton, and J. Xu, "A non-ordinary state-based peridynamic method to model solid material deformation and fracture," (in English), *International Journal of Solids and Structures,* Article vol. 46, no. 5, pp. 1186-1195, Mar 2009.

[9] W. Gerstle, N. Sau, and S. Silling, "Peridynamic modeling of concrete structures," (in English), *Nuclear Engineering and Design,* Article; Proceedings Paper vol. 237, no. 12-13, pp. 1250-1258, Jul 2007.

[10] O. Weckner and N. A. N. Mohamed, "Viscoelastic material models in peridynamics," *Applied Mathematics and Computation,* vol. 219, no. 11, pp. 6039-6043, 2013.

[11] Y. Mikata, "Analytical solutions of peristatic and peridynamic problems for a 1D infinite rod," *International Journal of Solids and Structures,* vol. 49, no. 21, pp. 2887-2897, 2012.

[12] O. Weckner, G. Brunk, M. A. Epton, S. A. Silling, and E. Askari, "Green's functions in non-local three-dimensional linear elasticity," in *Proceedings of the Royal Society of London A: Mathematical, Physical and Engineering Sciences*, 2009, p. rspa20090234: The Royal Society.

[13] B. Aksoylu and Z. Unlu, "Conditioning analysis of nonlocal integral operators in fractional Sobolev spaces," *SIAM Journal on Numerical Analysis,* vol. 52, no. 2, pp. 653-677, 2014.

[14] W. Liu and J.-W. Hong, "A coupling approach of discretized peridynamics with finite element method," *Computer Methods in Applied Mechanics and Engineering,* vol. 245, pp. 163-175, 2012.

[15] B. Kilic and E. Madenci, "Coupling of peridynamic theory and the finite element method," *Journal of mechanics of materials and structures,* vol. 5, no. 5, pp. 707-733, 2010.

[16] R. A. Wildman and G. A. Gazonas, "A finite difference-augmented peridynamics method for reducing wave dispersion," *International Journal of Fracture,* vol. 190, no. 1-2, pp. 39-52, 2014.

[17] G. Lubineau, Y. Azdoud, F. Han, C. Rey, and A. Askari, "A morphing strategy to couple non-local to local continuum mechanics," *Journal of the Mechanics and Physics of Solids,* vol. 60, no. 6, pp. 1088-1102, 2012.

[18] S. Silling, D. Littlewood, and P. Seleson, "Variable horizon in a peridynamic medium," *Journal of Mechanics of Materials and Structures,* vol. 10, no. 5, pp. 591-612, 2015.

[19] P. Seleson, S. Beneddine, and S. Prudhomme, "A force-based coupling scheme for peridynamics and classical elasticity," *Computational Materials Science,* vol. 66, pp. 34-49, 2013.

[20] B. Ren, H. Fan, G. L. Bergel, R. A. Regueiro, X. Lai, and S. Li, "A peridynamics–SPH coupling approach to simulate soil fragmentation induced by shock waves," *Computational Mechanics,* vol. 55, no. 2, pp. 287-302, 2015.

[21] H. Fan, G. L. Bergel, and S. Li, "A hybrid peridynamics–SPH simulation of soil fragmentation by blast loads of buried explosive," *International Journal of Impact Engineering,* vol. 87, pp. 14-27, 2016.

[22] F. Xu, M. Gunzburger, J. Burkardt, and Q. Du, "A multiscale implementation based on adaptive mesh refinement for the nonlocal peridynamics model in one dimension," *Multiscale Modeling & Simulation,* vol. 14, no. 1, pp. 398-429, 2016.

[23] Y. D. Ha, J. Lee, and J.-W. Hong, "Fracturing patterns of rock-like materials in compression captured with peridynamics," *Engineering Fracture Mechanics,* vol. 144, pp. 176-193, 2015.

[24] F. Bobaru and Y. D. Ha, "Adaptive refinement and multiscale modeling in 2D peridynamics," 2011.

[25] S. A. Silling and R. B. Lehoucq, "Convergence of peridynamics to classical elasticity theory," *Journal of Elasticity,* vol. 93, no. 1, pp. 13-37, 2008.

[26] F. Bobaru, M. Yang, L. F. Alves, S. A. Silling, E. Askari, and J. Xu, "Convergence, adaptive refinement, and scaling in 1D peridynamics," *International Journal for Numerical Methods in Engineering,* vol. 77, no. 6, pp. 852-877, 2009.

[27] P. Seleson and D. J. Littlewood, "Convergence studies in meshfree peridynamic simulations," *Computers & Mathematics with Applications*, vol. 71, no. 11, pp. 2432-2448, 2016.

[28] P. Seleson and M. Parks, "On the role of the influence function in the peridynamic theory," *International Journal of Multiscale Computational Engineering*, vol. 9, no. 6, pp. 689-706, 2011.

[29] E. Askari, F. Bobaru, R. Lehoucq, M. Parks, S. Silling, and O. Weckner, "Peridynamics for multiscale materials modeling," in *Journal of Physics: Conference Series*, 2008, vol. 125, no. 1, p. 012078: IOP Publishing.

[30] F. Bobaru, "Peridynamics and multiscale modeling," *International Journal for Multiscale Computational Engineering*, vol. 9, no. 6, 2011.

[31] S. A. Silling and F. Bobaru, "Peridynamic modeling of membranes and fibers," *International Journal of Non-Linear Mechanics*, vol. 40, no. 2, pp. 395-409, 2005.

[32] F. Bobaru, S. A. Silling, and H. Jiang, "Peridynamic fracture and damage modeling of membranes and nanofiber networks," in *XI Int. Conf. Fract., Turin, Italy*, 2005.

[33] S. Ebrahimi, D. Steigmann, and K. Komvopoulos, "Peridynamics analysis of the nanoscale friction and wear properties of amorphous carbon thin films," *Journal of Mechanics of Materials and Structures*, vol. 10, no. 5, pp. 559-572, 2015.

[34] C. J. Lammi, T. J. Vogler, M. L. Elert, W. T. Buttler, J. P. Borg, and J. L. Jordan, "Mesoscale simulations of granular materials with peridynamics," in *AIP Conference Proceedings*, 2012, vol. 1426, no. 1, pp. 1467-1470: AIP.

[35] R. B. Lehoucq and S. A. Silling, "Statistical coarse-graining of molecular dynamics into peridynamics," *Report SAND2007-6410, Sandia National Laboratories, Albuquerque, New Mexico*, 2007.

[36] P. Seleson, M. L. Parks, M. Gunzburger, and R. B. Lehoucq, "Peridynamics as an upscaling of molecular dynamics," *Multiscale Modeling & Simulation,* vol. 8, no. 1, pp. 204-227, 2009.

[37] N. I. Jacob and N. Israelachvili, "Intermolecular and surface forces," *San Diego: Academic,* 1992.

[38] S. A. Silling and E. Askari, "A meshfree method based on the peridynamic model of solid mechanics," (in English), *Computers & Structures,* Article; Proceedings Paper vol. 83, no. 17-18, pp. 1526-1535, Jun 2005.

[39] J. T. Foster, S. A. Silling, and W. W. Chen, "State based peridynamic modeling of dynamic fracture," in *SEM Annual Conf and Exposition on Experimental and Applied Mechanics, Albuquerque, USA,* 2009, pp. 2312-2317.

[40] F. Bobaru and G. Zhang, "Why do cracks branch? A peridynamic investigation of dynamic brittle fracture," *International Journal of Fracture,* vol. 196, no. 1-2, pp. 59-98, 2015.

[41] Y. D. Ha and F. Bobaru, "Characteristics of dynamic brittle fracture captured with peridynamics," *Engineering Fracture Mechanics,* vol. 78, no. 6, pp. 1156-1168, 2011.

[42] M. J. Buehler and H. Gao, "Dynamical fracture instabilities due to local hyperelasticity at crack tips," *Nature,* vol. 439, no. 7074, pp. 307-310, 2006.

[43] Y. D. Ha and F. Bobaru, "Studies of dynamic crack propagation and crack branching with peridynamics," *International Journal of Fracture,* vol. 162, no. 1, pp. 229-244, 2010.

[44] F. Bobaru and W. Hu, "The meaning, selection, and use of the peridynamic horizon and its relation to crack branching in brittle materials," *International Journal of Fracture,* pp. 1-8, 2012.

[45] A. Agwai, I. Guven, and E. Madenci, "Predicting crack propagation with peridynamics: a comparative study," *International Journal of Fracture,* vol. 171, no. 1, pp. 65-78, 2011.

[46] D. Dipasquale, M. Zaccariotto, and U. Galvanetto, "Crack propagation with adaptive grid refinement in 2D peridynamics," *International Journal of Fracture,* vol. 190, no. 1-2, pp. 1-22, 2014.

[47] F. Wang, L. Liu, Q. Liu, D. Cao, and S. Yang, "Studies of Bimaterial Interface Fracture with Peridynamics," 2015.

[48] W. Gerstle, N. Sau, and S. Silling, "Peridynamic modeling of plain and reinforced concrete structures," in *SMiRT18, Int. Conf. Structural Mech. Reactor Technol*, 2005.

[49] F. Shen, Q. Zhang, and D. Huang, "Damage and failure process of concrete structure under uniaxial compression based on peridynamics modeling," *Mathematical Problems in Engineering,* vol. 2013, 2013.

[50] D. Huang, Q. Zhang, and P. Qiao, "Damage and progressive failure of concrete structures using non-local peridynamic modeling," *Science China Technological Sciences,* vol. 54, no. 3, pp. 591-596, 2011.

[51] A. Yaghoobi and M. G. Chorzepa, "Meshless modeling framework for fiber reinforced concrete structures," *Computers & Structures,* vol. 161, pp. 43-54, 2015.

[52] Z. Q. Cheng, G. F. Zhang, Y. N. Wang, and F. Bobaru, "A peridynamic model for dynamic fracture in functionally graded materials," (in English), *Composite Structures,* Article vol. 133, pp. 529-546, Dec 2015.

[53] M. Ghajari, L. Iannucci, and P. Curtis, "A peridynamic material model for the analysis of dynamic crack propagation in orthotropic media," *Computer Methods in Applied Mechanics and Engineering,* vol. 276, pp. 431-452, 2014.

[54] D. De Meo, C. Diyaroglu, N. Zhu, E. Oterkus, and M. A. Siddiq, "Modelling of stress-corrosion cracking by using peridynamics," (in English), *International Journal of Hydrogen Energy,* Article vol. 41, no. 15, pp. 6593-6609, Apr 2016.

[55] Z. Chen and F. Bobaru, "Peridynamic modeling of pitting corrosion damage," *Journal of the Mechanics and Physics of Solids,* vol. 78, pp. 352-381, 2015.

[56] E. Oterkus, I. Guven, and E. Madenci, "Fatigue failure model with peridynamic theory," in *Thermal and Thermomechanical Phenomena in Electronic Systems (ITherm), 2010 12th IEEE Intersociety Conference on*, 2010, pp. 1-6: IEEE.

[57] S. A. Silling and A. Askari, "Peridynamic model for fatigue cracking," *SAND2014-18590. Albuquerque: Sandia National Laboratories,* 2014.

[58] G. Zhang, Q. Le, A. Loghin, A. Subramaniyan, and F. Bobaru, "Validation of a peridynamic model for fatigue cracking," *Engineering Fracture Mechanics,* vol. 162, pp. 76-94, 2016.

[59] J. T. Foster, S. A. Silling, and W. Chen, "An energy based failure criterion for use with peridynamic states," *International Journal for Multiscale Computational Engineering,* vol. 9, no. 6, 2011.

[60] S. Nadimi, I. Miscovic, and J. McLennan, "A 3D peridynamic simulation of hydraulic fracture process in a heterogeneous medium," (in English), *Journal of Petroleum Science and Engineering,* Article vol. 145, pp. 444-452, Sep 2016.

[61] B. Kilic and E. Madenci, "Structural stability and failure analysis using peridynamic theory," (in English), *International Journal of Non-Linear Mechanics,* Article vol. 44, no. 8, pp. 845-854, Oct 2009.

[62] S. Oterkus and E. Madenci, "PERIDYNAMICS FOR ANTIPLANE SHEAR AND TORSIONAL DEFORMATIONS," (in English), *Journal of Mechanics of Materials and Structures,* Article vol. 10, no. 2, pp. 167-193, Mar 2015.

[63] M.-Y. Moon, J.-H. Kim, Y. D. Ha, and S. Cho, "Adjoint design sensitivity analysis of dynamic crack propagation using peridynamic theory," *Structural and Multidisciplinary Optimization*, vol. 51, no. 3, pp. 585-598, 2015.

[64] R. Lipton, "Cohesive dynamics and brittle fracture," *Journal of Elasticity*, vol. 124, no. 2, pp. 143-191, 2016.

[65] W. Hu, Y. D. Ha, and F. Bobaru, "Modeling dynamic fracture and damage in a fiber-reinforced composite lamina with peridynamics," *International Journal for Multiscale Computational Engineering*, vol. 9, no. 6, 2011.

[66] J. Xu, A. Askari, O. Weckner, and S. Silling, "Peridynamic analysis of impact damage in composite laminates," *Journal of Aerospace Engineering*, vol. 21, no. 3, pp. 187-194, 2008.

[67] W. Hu, Y. D. Ha, and F. Bobaru, "Peridynamic model for dynamic fracture in unidirectional fiber-reinforced composites," *Computer Methods in Applied Mechanics and Engineering*, vol. 217, pp. 247-261, 2012.

[68] B. Kilic, A. Agwai, and E. Madenci, "Peridynamic theory for progressive damage prediction in center-cracked composite laminates," *Composite Structures*, vol. 90, no. 2, pp. 141-151, 2009.

[69] Y. Hu, N. De Carvalho, and E. Madenci, "Peridynamic modeling of delamination growth in composite laminates," *Composite Structures*, vol. 132, pp. 610-620, 2015.

[70] C. Sun and Z. Huang, "Peridynamic simulation to impacting damage in composite laminate," *Composite Structures*, vol. 138, pp. 335-341, 2016.

[71] E. Oterkus and E. Madenci, "Peridynamic analysis of fiber-reinforced composite materials," *Journal of Mechanics of Materials and Structures*, vol. 7, no. 1, pp. 45-84, 2012.

[72] Y. Hu and E. Madenci, "Bond-based peridynamic modeling of composite laminates with arbitrary fiber orientation and stacking sequence," *Composite structures,* vol. 153, pp. 139-175, 2016.

[73] Y. Hu and E. Madenci, "Bond-based peridynamics with an arbitrary poisson's ratio," in *57th AIAA/ASCE/AHS/ASC Structures, Structural Dynamics, and Materials Conference*, 2016, p. 1722.

[74] C. Diyaroglu, E. Oterkus, E. Madenci, T. Rabczuk, and A. Siddiq, "Peridynamic modeling of composite laminates under explosive loading," *Composite Structures,* vol. 144, pp. 14-23, 2016.

[75] H. Ouchi, A. Katiyar, J. York, J. T. Foster, and M. M. Sharma, "A fully coupled porous flow and geomechanics model for fluid driven cracks: a peridynamics approach," *Computational Mechanics,* vol. 55, no. 3, pp. 561-576, 2015.

[76] R. Jabakhanji and R. H. Mohtar, "A peridynamic model of flow in porous media," *Advances in Water Resources,* vol. 78, pp. 22-35, 2015.

[77] R. T. Haftka and R. V. Grandhi, "STRUCTURAL SHAPE OPTIMIZATION - A SURVEY," (in English), *Computer Methods in Applied Mechanics and Engineering,* Article vol. 57, no. 1, pp. 91-106, Aug 1986.

[78] M. P. Bendsoe and N. Kikuchi, "GENERATING OPTIMAL TOPOLOGIES IN STRUCTURAL DESIGN USING A HOMOGENIZATION METHOD," (in English), *Computer Methods in Applied Mechanics and Engineering,* Article vol. 71, no. 2, pp. 197-224, Nov 1988.

[79] G. Allaire and R. V. Kohn, "TOPOLOGY OPTIMIZATION AND OPTIMAL SHAPE DESIGN USING HOMOGENIZATION," (in English), *Topology Design of Structures,* Proceedings Paper vol. 227, pp. 207-218, 1993.

[80] M. P. Bendsoe, *Optimization of structural topology, shape, and material*. Springer, 1995.

[81] G. Rozvany and M. Zhou, "Applications of the COC algorithm in layout optimization," in *Engineering optimization in design processes*: Springer, 1991, pp. 59-70.

[82] G. Rozvany and M. Zhou, "The COC algorithm, part I: cross-section optimization or sizing," *Computer Methods in Applied Mechanics and Engineering,* vol. 89, no. 1-3, pp. 281-308, 1991.

[83] M. Zhou and G. Rozvany, "The COC algorithm, Part II: Topological, geometrical and generalized shape optimization," *Computer Methods in Applied Mechanics and Engineering,* vol. 89, no. 1-3, pp. 309-336, 1991.

[84] G. I. N. Rozvany, M. Zhou, and T. Birker, "GENERALIZED SHAPE OPTIMIZATION WITHOUT HOMOGENIZATION," (in English), *Structural Optimization,* Note vol. 4, no. 3-4, pp. 250-252, Oct 1992.

[85] O. Sigmund, "Morphology-based black and white filters for topology optimization," (in English), *Structural and Multidisciplinary Optimization,* Article vol. 33, no. 4-5, pp. 401-424, Apr 2007.

[86] E. Andreassen, A. Clausen, M. Schevenels, B. S. Lazarov, and O. Sigmund, "Efficient topology optimization in MATLAB using 88 lines of code," (in English), *Structural and Multidisciplinary Optimization,* Article vol. 43, no. 1, pp. 1-16, Jan 2011.

[87] S. Osher and J. A. Sethian, "FRONTS PROPAGATING WITH CURVATURE-DEPENDENT SPEED - ALGORITHMS BASED ON HAMILTON-JACOBI FORMULATIONS," (in English), *Journal of Computational Physics,* Article vol. 79, no. 1, pp. 12-49, Nov 1988.

[88] J. A. Sethian and A. Wiegmann, "Structural boundary design via level set and immersed interface methods," (in English), *Journal of Computational Physics,* Article vol. 163, no. 2, pp. 489-528, Sep 2000.

[89] M. Y. Wang, X. Wang, and D. Guo, "A level set method for structural topology optimization," *Computer methods in applied mechanics and engineering*, vol. 192, no. 1, pp. 227-246, 2003.

[90] P. D. Dunning and H. A. Kim, "Introducing the sequential linear programming level-set method for topology optimization," (in English), *Structural and Multidisciplinary Optimization*, Article vol. 51, no. 3, pp. 631-643, Mar 2015.

[91] H. A. Eschenauer, V. V. Kobelev, and A. Schumacher, "BUBBLE METHOD FOR TOPOLOGY AND SHAPE OPTIMIZATION OF STRUCTURES," (in English), *Structural Optimization*, Article vol. 8, no. 1, pp. 42-51, Aug 1994.

[92] H. Eschenauer and A. Schumacher, "Topology and shape optimization procedures using hole positioning criteria," in *Topology optimization in structural mechanics*: Springer, 1997, pp. 135-196.

[93] Y. M. Xie and G. P. Steven, "A SIMPLE EVOLUTIONARY PROCEDURE FOR STRUCTURAL OPTIMIZATION," (in English), *Computers & Structures*, Note vol. 49, no. 5, pp. 885-896, Dec 1993.

[94] Y. M. Xie and G. P. Steven, *Evolutionary structural optimization*. Springer, 2012.

[95] X. Y. Yang, Y. M. Xie, G. P. Steven, and O. M. Querin, "Bidirectional evolutionary method for stiffness optimization," (in English), *Aiaa Journal*, Article; Proceedings Paper vol. 37, no. 11, pp. 1483-1488, Nov 1999.

[96] X. Huang and M. Xie, *Evolutionary topology optimization of continuum structures: methods and applications*. John Wiley & Sons, 2010.

[97] E. Biyikli and A. C. To, "Proportional Topology Optimization: A New Non-Sensitivity Method for Solving Stress Constrained and Minimum Compliance Problems and Its Implementation in MATLAB," (in English), *Plos One*, Article vol. 10, no. 12, p. 23, Dec 2015, Art. no. e0145041.

[98] J. Kim, *Topology optimization for 2-D continuum using element free Galerkin method*. 1997.

[99] Z. Luo, N. Zhang, Y. Wang, and W. Gao, "Topology optimization of structures using meshless density variable approximants," (in English), *International Journal for Numerical Methods in Engineering,* Article vol. 93, no. 4, pp. 443-464, Jan 2013.

[100] Q. Z. He, Z. Kang, and Y. Q. Wang, "A topology optimization method for geometrically nonlinear structures with meshless analysis and independent density field interpolation," (in English), *Computational Mechanics,* Article vol. 54, no. 3, pp. 629-644, Sep 2014.

[101] J. Lin, Y. Guan, G. Zhao, H. Naceur, and P. Lu, "Topology optimization of plane structures using smoothed particle hydrodynamics method," *International Journal for Numerical Methods in Engineering,* 2016.

[102] S. Li and S. Atluri, "Topology-optimization of structures based on the MLPG mixed collocation method," *COMPUTER MODELING IN ENGINEERING AND SCIENCES,* vol. 26, no. 1, p. 61, 2008.

[103] S. Y. Wang, K. Tai, and M. Y. Wang, "An enhanced genetic algorithm for structural topology optimization," (in English), *International Journal for Numerical Methods in Engineering,* Article vol. 65, no. 1, pp. 18-44, Jan 2006.

[104] S. Y. Wang and K. Tai, "Structural topology design optimization using Genetic Algorithms with a bit-array representation," (in English), *Computer Methods in Applied Mechanics and Engineering,* Article vol. 194, no. 36-38, pp. 3749-3770, 2005.

[105] S. Bureerat and J. Limtragool, "Structural topology optimisation using simulated annealing with multiresolution design variables," (in English), *Finite Elements in Analysis and Design,* Article vol. 44, no. 12-13, pp. 738-747, Aug 2008.

[106] K. Svanberg and M. Werme, "Sequential integer programming methods for stress constrained topology optimization," (in English), *Structural and Multidisciplinary Optimization,* Article vol. 34, no. 4, pp. 277-299, Oct 2007.

[107] P. Underwood, "Dynamic relaxation(in structural transient analysis)," *Computational methods for transient analysis(A 84-29160 12-64). Amsterdam, North-Holland, 1983*, pp. 245-265, 1983.

[108] A. Shukla, A. Misra, and S. Kumar, "Checkerboard Problem in Finite Element Based Topology Optimization," *International Journal of Advances in Engineering & Technology,* vol. 6, no. 4, p. 1769, 2013.

[109] L. Li and K. Khandelwal, "Volume preserving projection filters and continuation methods in topology optimization," (in English), *Engineering Structures,* Article vol. 85, pp. 144-161, Feb 2015.

[110] C. Diyaroglu, E. Oterkus, S. Oterkus, and E. Madenci, "Peridynamics for bending of beams and plates with transverse shear deformation," (in English), *International Journal of Solids and Structures,* Article vol. 69-70, pp. 152-168, Sep 2015.